The newfirm medium-band survey: photometric catalogs, redshifts, and the bimodal color distribution of galaxies out to z 3

Journal Item

The Astrophysical Journal, 735:86 (21pp), 2011 July 10 doi:10.1088/0004-637X/735/2/86

THE NEWFIRM MEDIUM-BAND SURVEY: PHOTOMETRIC CATALOGS, REDSHIFTS, AND THE BIMODAL COLOR DISTRIBUTION OF GALAXIES OUT TO $z \sim 3$

Katherine E. Whitaker[1,10], Ivo Labbé[2,10], Pieter G. van Dokkum[1,10], Gabriel Brammer[1,3,10], Mariska Kriek[4,5,10], Danilo Marchesini[6,10], Ryan F. Quadri[7,10], Marijn Franx[7], Adam Muzzin[1,10], Rik J. Williams[2,10], Rachel Bezanson[1], Garth D. Illingworth[8], Kyoung-Soo Lee[1,10], Britt Lundgren[1], Erica J. Nelson[1], Gregory Rudnick[9,10], Tomer Tal[1], and David A. Wake[1]

[1] Department of Astronomy, Yale University, New Haven, CT 06511, USA; katherine.whitaker@yale.edu
[2] Carnegie Observatories, Pasadena, CA 91101, USA
[3] European Southern Observatory, Alonso de Córdova 3107, Casilla 19001, Vitacura, Santiago, Chile
[4] Department of Astrophysical Sciences, Princeton University, Princeton, NJ 08544, USA
[5] Harvard-Smithsonian Center for Astrophysics, Cambridge, MA 02138, USA
[6] Department of Physics and Astronomy, Tufts University, Medford, MA 02155, USA
[7] Sterrewacht Leiden, Leiden University, NL-2300 RA Leiden, The Netherlands
[8] UCO/Lick Observatory, Pasadena, CA 91101, USA
[9] Department of Physics and Astronomy, University of Kansas, Lawrence, KS 66045, USA
Received 2010 October 12; accepted 2011 May 6; published 2011 June 20

ABSTRACT

We present deep near-IR (NIR) medium-bandwidth photometry over the wavelength range 1–1.8 μm in the All-wavelength Extended Groth strip International Survey (AEGIS) and Cosmic Evolution Survey (COSMOS) fields. The observations were carried out using the NOAO Extremely Wide-Field Infrared Imager (NEWFIRM) on the Mayall 4 m Telescope on Kitt Peak as part of the NEWFIRM Medium-Band Survey (NMBS), an NOAO survey program. In this paper, we describe the full details of the observations, data reduction, and photometry for the survey. We also present a public *K*-selected photometric catalog, along with accurate photometric redshifts. The redshifts are computed with 37 (20) filters in the COSMOS (AEGIS) fields, combining the NIR medium-bandwidth data with existing UV (*Galaxy Evolution Explorer*), visible and NIR (Canada–France–Hawaii Telescope and Subaru Telescope), and mid-IR (*Spitzer*/IRAC) imaging. We find excellent agreement with publicly available spectroscopic redshifts, with $\sigma_z/(1+z) \sim 1\%$–2% for ∼4000 galaxies at $z = 0$–3. The NMBS catalogs contain ∼13,000 galaxies at $z > 1.5$ with accurate photometric redshifts and rest-frame colors. Due to the increased spectral resolution obtained with the five NIR medium-band filters, the median 68% confidence intervals of the photometric redshifts of both quiescent and star-forming galaxies are a factor of about two times smaller when comparing catalogs with medium-band NIR photometry to NIR broadband photometry. We show evidence for a clear bimodal color distribution between quiescent and star-forming galaxies that persists to $z \sim 3$, a higher redshift than has been probed so far.

Key words: catalogs – galaxies: distances and redshifts – galaxies: high-redshift – surveys

Online-only material: color figures

1. INTRODUCTION

The growing number of deep, wide-field multiwavelength surveys over multiple bands in the past decade has led to new insights into the physical processes that govern galaxy formation and evolution. With the advent of larger ground-based telescopes with improved near-IR (NIR) cameras and a new generation of space-based telescopes, surveys have pushed toward higher redshifts and further down the luminosity and mass functions. Although broadband photometric surveys of statistically significant samples of galaxies now span large portions of cosmic time, a fundamental limitation exists: the accuracy of the photometric redshift estimates. Accurate photometric redshifts are necessary to measure reliable rest-frame colors, stellar population properties, and environmental densities.

Deep optical medium-band photometric surveys such as the Classifying Object by Medium-Band Observations-17 (COMBO-17; Wolf et al. 2003) and the Cosmic Evolution Survey (COSMOS) with 30 bands (Ilbert et al. 2009) have photometric redshift accuracies of $\sigma_{\Delta z/(1+z_{\rm spec})} \sim 1\%$ for large samples of galaxies out to $z \sim 1$. By using medium-bandwidth filters, these surveys have improved the accuracy of photometric redshifts by factors of two to three.

As prominent rest-frame optical spectral features—notably the 4000 Å break—are shifted into the NIR at $z > 1.5$, most studies at high redshift have focused on those galaxies that are relatively bright at observed optical (rest-frame UV) wavelengths (e.g., Steidel et al. 1996, 1999). Consequently, these studies have missed relatively red galaxies (see, e.g., Franx et al. 2003; van Dokkum et al. 2006). Concessions must be made for studies of complete samples of high-redshift galaxies, where one can either work with small, bright spectroscopic samples (Cimatti et al. 2002; Kriek et al. 2008b) or use large samples that rely on less accurate broadband photometric redshifts (e.g., Dickinson et al. 2003; Fontana et al. 2006, and many other studies).

Here, following previous medium-band surveys in the optical, we extend the redshift range of accurate photometric redshifts out to $z \sim 3$ using medium-band NIR filters. The NOAO Extremely Wide-Field Infrared Imager (NEWFIRM)

[10] Visiting Astronomer, Kitt Peak National Observatory, National Optical Astronomy Observatory, which is operated by the Associations of Universities for Research in Astronomy (AURA) under cooperative agreement with the National Science Foundation.

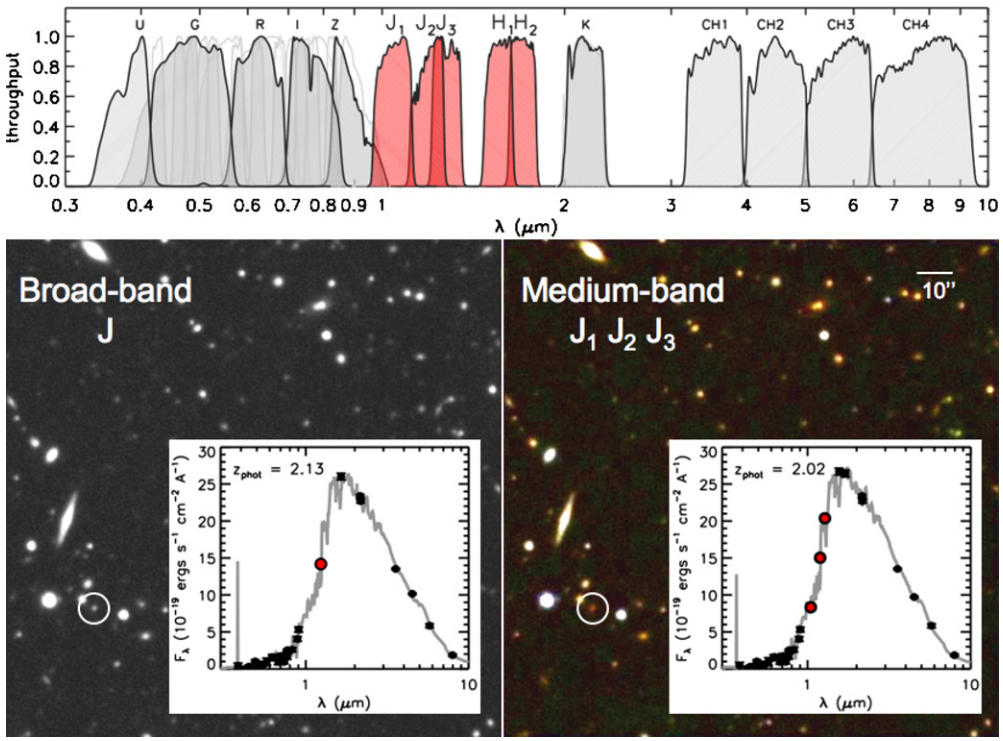

Figure 1. Small region of the COSMOS field (roughly 2′ on a side), shown for a broadband J filter (left) and a three-color image from the medium-band J_1, J_2, and J_3 filters (right). The red object in the bottom left of the image highlights the spectral features that we are able to resolve within only 0.2 μm in wavelength (see inset SED). The J filters trace out the Balmer/4000 Å break with higher resolution than the standard broadband filter, allowing for an accurate photometric redshift of this quiescent galaxy at $z = 2.02$. The normalized transmission curves of the filters in the NMBS catalogs are shown in the top panel; the additional COSMOS filters (e.g., the Subaru optical medium-band filters) are shown in gray scale behind the five optical filters.

(A color version of this figure is available in the online journal.)

Medium-Band Survey (NMBS) is a 75 night NOAO survey program on the Kitt Peak Mayall 4 m Telescope (Mayall).

An outline of the paper is as follows. We introduce the details of the NMBS in Section 2 and describe the image processing and optimization in Section 3. The source detection and photometry are described next in Section 4, elaborating on all of the details involved in extracting the NMBS catalogs. In Section 4.10, we compare the NMBS catalogs to other publicly available catalogs within the fields, finding good agreement. We derive photometric redshifts and rest-frame colors in Section 5 and show that the accurate redshifts and colors enable us to identify quiescent galaxies out to $z \sim 3$ in Section 6. Finally, we demonstrate the improvements enabled by the medium-bandwidth filters relative to the standard broadband filters by comparing the confidence intervals of the photometric redshifts in Section 7. A summary of the survey can be found in Section 8.

We assume a ΛCDM cosmology with $\Omega_M = 0.3$, $\Omega_\Lambda = 0.7$, and $H_0 = 70$ km s^{-1} Mpc^{-1} throughout the paper. All magnitudes are given in the AB system.

2. THE NEWFIRM MEDIUM-BAND SURVEY

The NMBS employs a new technique of using medium-bandwidth NIR filters to sample the Balmer/4000 Å break from $1.5 < z < 3.5$ at a higher resolution than the standard broadband NIR filters (van Dokkum et al. 2009), thereby improving the accuracy of photometric redshifts. A custom set of five medium-bandwidth filters in the wavelength range of 1–1.8 μm was fabricated for the NEWFIRM camera on Mayall for the NMBS. The J_1 band is similar to the Y band, the canonical J band is split into two filters, J_2 and J_3, and the H band is split into two filters, H_1 and H_2 (see the top panel in Figure 1). The full details of the medium-band filters can be found in van Dokkum et al. (2009).

Figure 1 demonstrates the power of the medium-band filters, comparing a traditional J-band image to a three-color image comprised of the J_1, J_2, and J_3 filters. Although the wavelength range of the three medium-bandwidth J filters only covers 0.2 μm, the filters are able to resolve strong spectral features such as Balmer/4000 Å breaks or emission lines. For example, J_1, J_2, and J_3 trace out the 4000 Å break of the massive, quiescent galaxies at $z = 2.02$ shown in Figure 1. When using the broadband J and H filters alone, the photometric redshift uncertainty is ∼4% in $(z_{\rm NMBS} - z_{\rm broadband})/(1 + z_{\rm NMBS})$, typical of the inherent uncertainties associated with broadband photometric redshifts. Through sampling the Balmer/4000 Å break region of the spectral energy distributions (SEDs) of the galaxies at $1.5 < z < 3.5$ with higher resolution, the uncertainties in the photometric redshifts and rest-frame colors decrease by about a factor of two (see Section 7).

2.1. Field Selection

The survey targets two fields within COSMOS (Scoville 2007) and the All-wavelength Extended Groth strip International Survey (AEGIS; Davis et al. 2007), chosen to take advantage of the wealth of publicly available ancillary data over a broad wavelength range (see Section 3.6). The NEWFIRM 27.′6×27.′6 pointing within the COSMOS field is centered at $\alpha = 9^{\rm h}59^{\rm m}53.^{\rm s}3$, $\delta = +02^\circ24^{\rm m}08^{\rm s}$ (J2000). This pointing overlaps with the zCOSMOS deep redshift

Table 1
Summary of Observations

Field	Filter	On-sky Time[a] (hr)	Integration Time[b] (hr)	Image Quality[c] (″)	5σ Depth[d]	Aperture Correction[e]	Zero Point
AEGIS	J1	29.3	25.0	1.13	25.2	1.9	23.31
	J2	25.9	24.1	1.16	25.3	1.9	23.35
	J3	29.1	22.9	1.08	24.5	1.8	23.37
	H1	26.5	22.3	1.10	24.1	2.0	23.59
	H2	20.8	17.1	1.06	24.4	1.8	23.61
	K	22.2	12.8	1.08	24.2	1.9	23.85
COSMOS	J1	31.2	24.9	1.19	25.1	2.0	23.31
	J2	21.9	19.6	1.17	24.8	1.9	23.35
	J3	27.5	24.8	1.12	24.7	1.9	23.37
	H1	22.3	14.7	1.03	24.2	1.8	23.59
	H2	20.0	17.0	1.24	24.0	2.1	23.61
	K	17.0	11.8	1.08	24.2	1.9	23.85

Notes.
[a] The total on-sky time represents all usable data, including aborted sequences and frames outside of the weather specifications or seeing constraints.
[b] The total integration time represents only those frames that were included in the final combined mosaics.
[c] The direct measurement of the FWHM from IRAF, independent of a profile model. The derivative of the enclosed flux profile is computed and the peak of the azimuthally averaged radial profile is found, where the FWHM is twice the radius of the profile at half the peak value.
[d] These are 5σ depths in a circular aperture of 1.″5 diameter, which corresponds to a total magnitude that is about 0.7 mag brighter for point sources for a seeing of 1.″1.
[e] The aperture correction for a point source to convert the 5σ depths to total magnitudes.

survey (Lilly et al. 2007) and the upcoming Ultra-VISTA survey.[11] The pointing in the AEGIS field is centered at $\alpha = 14^{h}18^{m}00^{s}$, $\delta = +52^{\circ}36^{m}07^{s}$ (J2000).

2.2. Observations

The observations were carried out with Mayall using the NEWFIRM camera with the J_1, J_2, J_3, H_1, and H_2 medium-bandwidth filters and the K broadband filter. Data were taken over the 2008A, 2008B, and 2009A semesters, for a total of 75 nights. The two main fields were observed whenever conditions were reasonable (i.e., no significant cirrus and seeing typically $<1.''5$), and they were available at an airmass <2 and $>20^{\circ}$ away from the moon.

Due to the dominance and short-term variability of the sky background, ground-based NIR imaging requires many short dithered exposures. This observing procedure is well established (see, e.g., Labbé et al. 2003; Quadri et al. 2007), and facilitates the removal of artifacts remaining from bright objects that can leave residual images in subsequent exposures. The telescope follows a semi-random dither pattern with a dither box of 90″, enabling good background subtraction without significantly reducing the area with maximal exposure. The dither box is sufficiently large to "fill in" the gaps between the four NEWFIRM arrays.

At each dither position, the exposure times were typically 1 × 60 s (co-adds × individual exposure time) for J_1, J_2, and J_3, 3 × 20 s for H_1 and H_2, and 5 × 12 s for K. The internally co-added frames make longer exposure times possible at each dither position while staying in the linear regime of the array.

We obtained a total on-sky integration time between 17 and 31 hr in each filter in each field over the three semesters (see Table 1 for details). This represents all usable data, including aborted sequences or frames that were outside weather specifications or seeing constraints; the total on-sky time was 294 hr. When tallying only those frames that get included in the final combined images, the total integration times range from 12 to 24 hr (a loss of ∼10%–30% of the data).

An overview of the median seeing and background levels measured in each observing sequence (ranging from 10 to 90 minutes, typically 60 minutes) is given in Figure 2. The median seeing is measured from bright stars in the individual frames that are fit with a two-dimensional (2D) Moffat model using the robust, nonlinear least-squares curve-fitting algorithm `mpfit` in IDL (Markwardt 2009). The data are of excellent quality with clean images that have no obvious systematic problems.

3. DATA REDUCTION

The data were reduced using a custom IDL code written by one of us (I.L.), following the method of the IRAF[12] package XDIMSUM.[13] The reduction process largely follows Labbé et al. (2003), Förster Schreiber et al. (2006), Quadri et al. (2007), and Taylor et al. (2009b). Below, we summarize the process, highlighting modifications to the standard process described in the papers listed above.

3.1. Image Processing

Every individual raw frame was visually inspected to identify any poor quality frames. To fall into this category, the frame must either (1) contain artifacts such as satellite streaks, ghost pupils or other transient features on the detector, (2) have a strongly varying background across the detector, (3) have severe elongation of the point-spread function (PSF), or (4) have double images of all objects due to "jumps" of the telescope or wind shake. Between 10% and 30% of the raw data was discarded for each filter, resulting in final combined mosaics with negligible artifacts.

The dark current is non-negligible in NIR cameras and thus dark images with the appropriate exposure times relative to the

[11] http://www.eso.org/sci/observing/policies/PublicSurveys/

[12] IRAF is distributed by the National Optical Astronomy Observatory, which is operated by the Association of Universities for Research in Astronomy, Inc., under cooperative agreement with the National Science Foundation.
[13] http://iraf.noao.edu/iraf/ftp/ftp/extern/

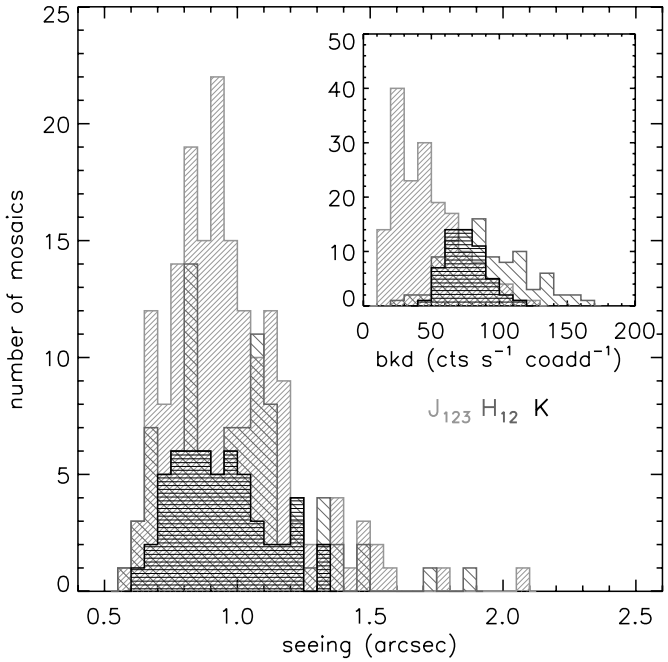

Figure 2. Median seeing, as implied by a Moffat fit, and sky background in the combined sequences (typically ∼60 minutes) for J_1, J_2, and J_3 (light gray), H_1 and H_2 (gray), and K (black).

co-added science images are subtracted. Next, the raw images must be divided by the flat-field image to remove variations in the sensitivity across the array.

We constructed flat fields from dome flats in combination with observations of the open cluster M67, accounting for both the small- and large-scale variations across the arrays, respectively. First, we determined the pixel-to-pixel response from dome flats. The large-scale structure in the dome flats was removed by median filtering using a 51 × 51 pixel box, fitting a seventh-order 2D Legendre polynomial to the median-filtered image, and dividing by this fit. It was verified that subtracting rather than dividing by the fit changes the resulting residual image by <1% (except for the K band, where differences can be up to ∼5% in the corners of the arrays).

The simple flat fields are not enough to correct to the large-scale sensitivity of the array due to imperfect illumination corrections. We therefore determine the sensitivity variations across each array from observations of the open cluster M67 in an 8 × 8 grid of positions spanning 28′ × 28′; this way, many stars were observed on many array positions. The M67 data were dark-subtracted, flat-fielded using the "flattened" dome flat (i.e., the dome flat with large-scale structure removed), and sky-subtracted. The fluxes of stars in M67 were measured using SExtractor (Bertin & Arnouts 1996) with a 4″ diameter aperture. Using the R.A. and decl. of the detected objects, sequences of unique stars imaged on multiple positions were identified. From these stars, a response image was generated reflecting the large-scale response of the arrays. The scatter in the best-fit response was typically 1%–3%, with larger errors possible in small areas for some array/filter combinations. These "response images" were then multiplied by the flattened dome flat to create the flat fields.

The individual dark-subtracted and flat-fielded frames are combined in two passes. During the first pass, the sky background is created for each science frame from a running median of the dithered sequence of the four preceding and four subsequent science images. Next, the dithered sky-subtracted images are cross-correlated with the central frame to determine the relative shifts of the individual frames. The relative flux scaling between the images is determined by measuring the flux of stars spread across the field. Finally, the images are shifted to a common reference frame using linear interpolation and are combined. All objects in the combined image are detected using a simple thresholding algorithm to generate an object mask. This mask is then shifted back into the reference frame of each individual science exposure, and the background subtraction process described above is repeated in a second pass, using a mean combined with cubic interpolation. The second pass is optimal for the background subtraction as the objects are masked out during the calculation of the running median.

3.2. Further Optimization

In the reduction, we mask out any dead or hot pixels (or generically "bad" pixels) using a custom master bad pixel file. Bad pixels have a nonlinear response and these bad pixels can be easily separated from "normal" functioning pixels during twilight. The signal of good pixels increases or decreases linearly with time, and so we fit the average flux of each quadrant as a function of the time with a linear function. Any dead or hot pixels will exhibit variable behavior, resulting in drastically different best-fit slopes compared to properly functioning pixels. We flag any pixels with deviations >15%. The final bad pixel file contains a flag for any pixel that has been flagged in at least two of the twilight sequences, in addition to the original bad pixel file from the NEWFIRM calibration library. Although we are conservative with the bad pixel file, the total fraction of bad pixels is still small (∼7%). Any remaining bad pixels in each individual science frame are removed with a sigma-clipping algorithm before combining the images within the reduction.

The nonlinearity of the NEWFIRM arrays increases with additional signal, reaching ∼5% at 10,000 ADU. Beyond this level, the nonlinearity increases very steeply as the detector approaches saturation at 12,000 ADU. Co-adding frames allows us to keep exposure times short, thereby avoiding this nonlinear regime, as does observing when the sky levels are relatively low in a particular filter. A nonlinearity correction is applied to all individual frames, using the following empirical equation:

$$y = x\left(1 + \frac{6.64 \times 10^{-6}}{nx}\right), \quad (1)$$

where x is the nonlinear (raw) frame, y is the nonlinearity corrected frame, n is the number of internally co-added frames, and 6.64×10^{-6} is the average coefficient for the four arrays.[14] The nonlinearity correction to the photometry is typically <1% for the majority of frames.

Another issue in NIR detectors is persistence images of bright objects, where the array has not completely recovered from the previous exposures. To alleviate this problem, we create a second object mask of the cores of the brightest objects. These are used to mask the pixels that contained the brightest objects in the previous two exposures in the final pass of the reduction. The detectors also exhibit bias residuals that are constant along rows. After masking all sources, the residual bias is removed by subtracting the median of each row in the individual sky-subtracted frames.

The final major optimization of the image combination includes weighting the individual sky-subtracted frames to

[14] http://www.noao.edu/staff/med/newfirm/fewompt/newfirm_linearity.pdf

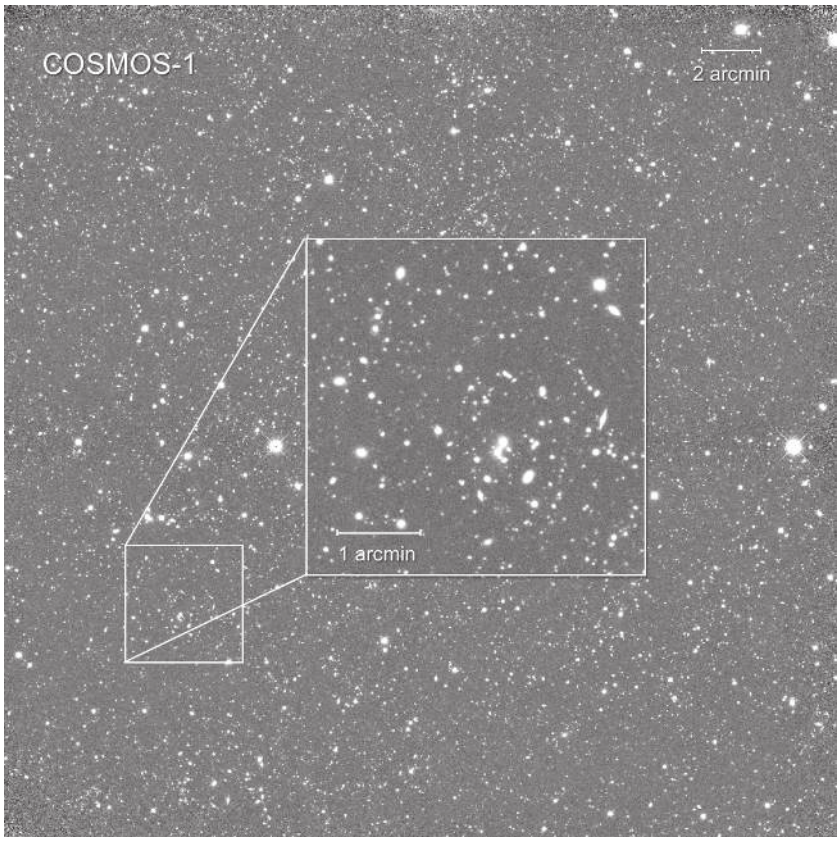

Figure 3. COSMOS *K*-band image, with a field of view of ∼30 × 30 arcmin. The background is both uniform and clean with no significant artifacts within the field that would affect the photometry.

maximize the signal-to-noise ratio (S/N; see, e.g., Labbé et al. 2003; Quadri et al. 2007). This method substantially improves the final image depth and quality by assigning weights to the individual frames that take into account variations in the seeing, sky transparency, background noise, and PSF ellipticity. To optimize the S/N, the weight is proportional to the square of the flux scale (scale$_i$) divided by the median sky background (sky$_i$) and the median size of the seeing disk (FWHM$_i$), penalized for ellipticity:

$$w_i = \frac{\text{scale}_i^2}{\text{sky}_i \times \frac{\text{FWHM}_i^2}{\sqrt{1-e^2}}}. \quad (2)$$

3.3. Astrometry

The weighted, sky-subtracted individual frames are combined into a single mosaic with a pixel scale of 0.″3 pixel^{-1} (resampled from the native NEWFIRM pixel scale of 0.″4 pixel^{-1}). The combined NMBS mosaics are aligned with the Canada–France–Hawaii Telescope (CFHT) *I*-band images (see Section 3.6), with an astrometric precision of $\lesssim$0.″1 over the entire field of view. The relative registration between the NMBS and CFHT images must be precise to allow for accurate colors and cross-identification of sources.

The initial registration within the code is performed using a linear transformation in the first pass of the reduction. The rms variation in the position of individual sources is about 0.″1–0.″2 (0.3–0.7 pixels) in most cases, but can be as high as $\gtrsim$0.5″–1″ (2–3 pixels) in the corners of the arrays. We fit the residual distortions with a second-order polynomial and combine this fit with the original transformation. This combined distortion correction is then applied to the images, which are registered using a cubic interpolation. The resulting rms variation in position of the individual sources in the final combined images is $\lesssim$0.″1 (0.3 pixels).

3.4. Photometric Calibration

NIR spectro-photometric standard stars from the Calibration Database System[15] were observed in wide five-point dither patterns on photometric nights in the 2008A semester. All of the other data were directly tied to the photometric data from 2008A. Synthetic magnitudes of these stars were calculated by integrating their observed (*Hubble Space Telescope* (*HST*)/NICMOS) spectra in the five medium-bandwidth filters (see Table 2 in van Dokkum et al. 2009). We adopt the mean zero points from these observations, listed in Table 1. The zero points derived from these standard stars are remarkably stable, with variations of $\lesssim$0.02 mag throughout the observing program.

A Galactic extinction correction has been applied to the photometry within the catalogs, as estimated from Schlegel et al. (1998). The corrections ranged from 4.5% to 0.3% for the $u - K$ photometry in the AEGIS field, with slightly larger values of 8%–0.6% in the COSMOS field due to its lower Galactic latitude.

3.5. Noise Properties

The final combined J_1, J_2, J_3, H_1, H_2, and K images constructed from the individually registered, distortion-corrected weighted averages of all frames are of excellent quality. The flatness of the background is readily visible in the final combined *K*-band images shown in Figures 3 and 4. Furthermore,

[15] http://www.stsci.edu/hst/observatory/cdbs/calspec.html

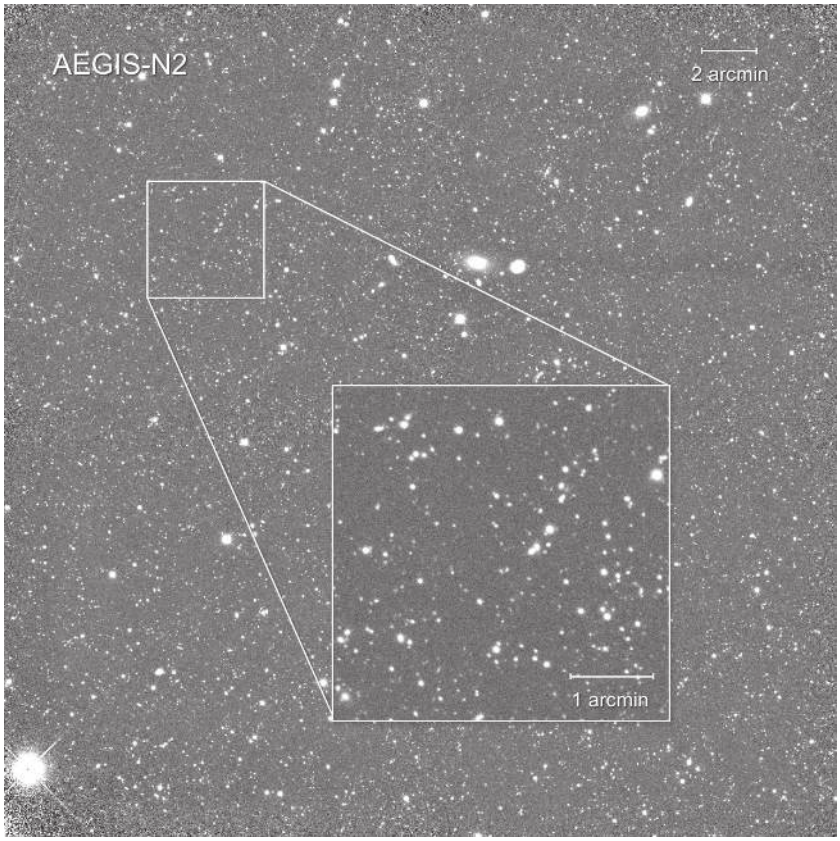

Figure 4. AEGIS *K*-band image (roughly ∼30 × 30 arcmin), with the inset demonstrating the quality and depth of the data.

the relatively deep and wide images are rich in compact sources. The combined images are slightly shallower near the edges and center of the image where there are gaps between the NEWFIRM arrays, as these areas receive less exposure time in the dither pattern. This is reflected in the weight maps containing the total exposure time per pixel. The reduced NMBS images and weight maps will be made publicly available through the NOAO archive.[16]

Well-understood noise properties are important both for calculating the depths of the final combined images and for measuring accurate photometric uncertainties. Although the noise properties of the raw images are well described by the variance of the signal per pixel, the reduction process introduces correlations between neighboring pixels. Additionally, small errors in the background subtraction may contribute to the noise.

To estimate the noise, we follow Labbé et al. (2005) and empirically fit the dependence of the normalized median absolute deviation (nmad) of the background as a function of the linear size N of an aperture with area A, where $N = \sqrt{A}$. We measure the fluxes in >1000 independent circular apertures randomly placed on the registered, sky-subtracted convolved images (see Section 4.1 for a description of the PSF matching) in a range of aperture sizes. Any apertures that overlap with the detection image segmentation map are excluded.

As described in Quadri et al. (2007), the scaling of the background noise with aperture size will be proportional to N^2 in the limiting case of perfect correlations between the pixels within an aperture. In the other extreme case of uncorrelated adjacent pixels within an aperture, the background noise scales with the linear size N. The latter standard relation is unrealistic given the correlations between pixels that were introduced by the imperfect background subtraction but also by undetected sources, resampling of the pixels, etc. The true scaling between the background and the linear size falls somewhere between these two extremes. Following Quadri et al. (2007), we parameterize the noise properties as

$$\sigma_{\rm nmad} = \sigma_1 \alpha N^{\beta}, \quad (3)$$

where $1 < \beta < 2$, σ_1 is the standard deviation of the background pixels, and α is the normalization. In Figure 5, we see that the width of the noise distribution within an aperture increases with increasing aperture size. The best-fit scaling of the background fluctuations falls roughly between the two extremes of no correlation and a perfect correlation from pixel to pixel, with a best-fit power-law index of $\beta = 1.37$ in COSMOS ($\beta = 1.35$ in AEGIS).

The background noise measurements are used to estimate the depths of the images. In Table 1, we list the 5σ limiting depths. These values are calculated using the background fluctuations within a 1.″5 "color" aperture (see Section 4.1). An additional aperture correction determined from the growth curves must be applied to these values to convert to total fluxes (see Column 7 of Table 1). The typical aperture correction for a point source is 1.9 for a typical seeing of ∼1.″1.

3.6. Ancillary Images

The survey catalog combines the data taken with the NEWFIRM camera with publicly available optical *ugriz* broadband images of both survey fields from the Deep Canada–France–Hawaii Telescope Legacy Survey

[16] http://archive.noao.edu/nsa/

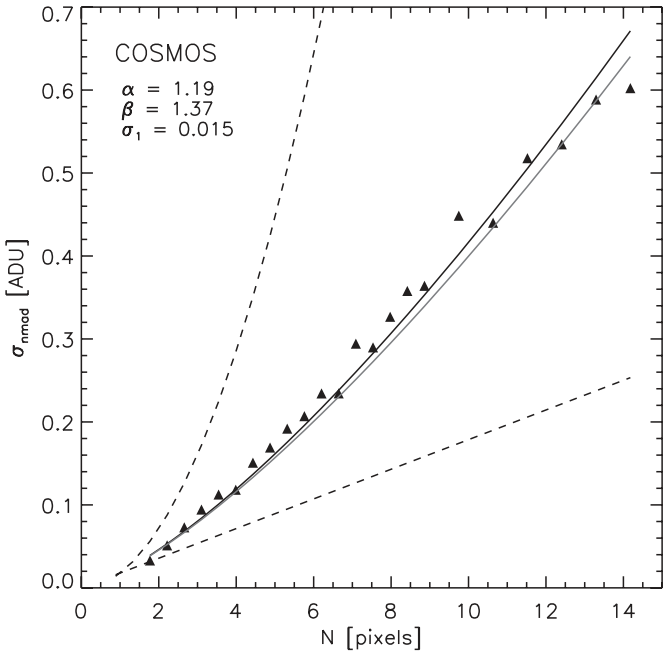

Figure 5. nmad value of background fluctuations for the COSMOS *K*-band image within an aperture with area *A* as a function of the linear size *N*, where $N = \sqrt{A}$. The filled triangles illustrate the measured values, whereas the black solid curve is the best fit to the data following the parameterization in Equation (3). The gray solid curve is the best fit to the AEGIS data (not shown here). The dashed curves show the expected scaling relations of the background fluctuations in the cases of no correlations among the pixels (bottom) and perfect correlations of all pixels within the aperture (top). Similar fits were performed for all filters in both fields.

(CFHTLS),[17] using image versions reduced by the CARS team (Erben et al. 2009; Hildebrandt et al. 2009), and JHK_S broadband imaging from the WIRCam Deep Survey (WIRDS; McCracken et al. 2010; R. Bielby et al. 2010, in preparation). Additionally, we include deep Subaru Telescope images with the B_J, V_J, r^+, i^+, and z^+ broadband filters and 12 medium-band filters in the COSMOS field (Taniguchi et al. 2007; Y. Taniguchi et al. 2008, in preparation).[18] We include mid-IR images in the *Spitzer*/IRAC bands over the entire COSMOS pointing that are provided by the S-COSMOS survey (Sanders et al. 2007), and partial coverage of the AEGIS pointing (∼0.15 deg^2) overlapping with the Extended Groth Strip (EGS; Barmby et al. 2008). The catalogs include *Spitzer*/MIPS fluxes at 24 μm that are derived from images provided by the S-COSMOS and Far-Infrared Deep Extragalactic Legacy[19] surveys, with the same coverage as the IRAC data. Finally, we incorporate near-UV (NUV) and Far-UV (FUV) *Galaxy Evolution Explorer* (*GALEX*; Martin et al. 2005) data in both fields from the Multimission Archive at the Space Telescope Science Institute into the catalogs (see also Zamojski et al. 2007 for a description of the COSMOS *GALEX* data).

All ancillary images are matched to the same pixel scale (0.″3 pixel^{-1}) and pointing of the NMBS images using the IRAF task `wregister`. The details of the source detection and extraction of photometry can be found in Section 4.2. In general, for objects that have flat spectra in F_λ, all of the ancillary data are deeper than the NMBS images with typical FWHM values of 0.″8 for the optical images. For consistent photometry in all (optical to NIR) bands, the images have all been convolved to the broadest PSF as determined from the growth curves (see Section 4.1 for more details).

[17] http://www.cfht.hawaii.edu/Science/CFHTLS/
[18] http://irsa.ipac.caltech.edu/data/COSMOS/images/
[19] http://irsa.ipac.caltech.edu/data/SPITZER/FIDEL/

4. PHOTOMETRY AND SOURCE DETECTION

We have 20 independent photometric filters in AEGIS, and in COSMOS we have 37 (FUV–8 μm). The optical and NIR images were convolved to the same PSF before performing aperture photometry so as to limit any bandpass-dependent effects. The source detection was done on the PSF-matched images with SExtractor (Bertin & Arnouts 1996) in relatively small apertures chosen to optimize the S/N (see Section 3.5). To extract the photometry from the ultraviolet and mid-IR images, we use an alternate source-fitting algorithm especially suited for heavily confused images for which a higher resolution prior (in this case, the *K*-band image) is available.

4.1. Optical and NIR PSF Matching

The FWHM of the PSF varies significantly between the optical and NIR bands; point sources in the optical images typically have FWHM of approximately 0.″8, whereas the point sources in the medium-band NIR images have FWHM of 1.″0–1.″2. Directly performing aperture photometry on these images would lead to different fractions of the flux falling within the aperture for different bands, thereby resulting in systematic color errors.

To minimize this problem, we degrade all of the optical and NIR images for each field to the broadest PSF. We produce high S/N PSFs for each band from bright (unsaturated) stars covering the entire field. Square postage stamps (32 pixels on a side or 9.″6) of the PSF stars are created, masking any nearby objects and averaged to create empirical PSFs. A kernel is then generated using the Lucy-Richardson method algorithm (`lucy` in IRAF) to convolve the empirical PSF to the broadest PSF (H_1 in AEGIS and H_2 in COSMOS).

Growth curves were determined for the empirical PSFs in each band, measuring the enclosed flux as a function of the aperture size. In the top panels of Figure 6, we show the ratio of the growth curves of each band relative to the broadest PSF in both fields before degrading the PSF (dashed lines). Generally, the broadest PSFs (the slowest-growing growth curves) are the longer wavelength bands. The bottom panels of Figure 6 show the ratio of the growth curves once they have been smoothed to the worst seeing. For "perfect" PSF matching, this ratio should be unity at all aperture diameters. At the aperture size used for the flux measurements (solid black line), the PSFs of all bands are matched within <2% for both fields.

Given the noise properties of the images (see Section 3.5) and the growth curve of the PSFs, we estimate the aperture size that optimizes the S/N for point sources in Figure 7. This optimization enables accurate color measurements, which are necessary for photometric redshift calculations and modeling of the stellar populations. We adopt an aperture of 5 pixels (1.″5), defining the color aperture as

$$F_{\mathrm{color},i} = \sum_{\sqrt{x^2+y^2}<0.''75} F_i(x, y), \quad (4)$$

where $F_{\mathrm{color},i}$ is the flux for each band *i* within a circular aperture with a radius $r = \sqrt{x^2 + y^2}$ of 0.″75. The color aperture defined in Equation (4) is small enough to give a nearly optimal S/N for point sources and large enough to minimize possible systematics

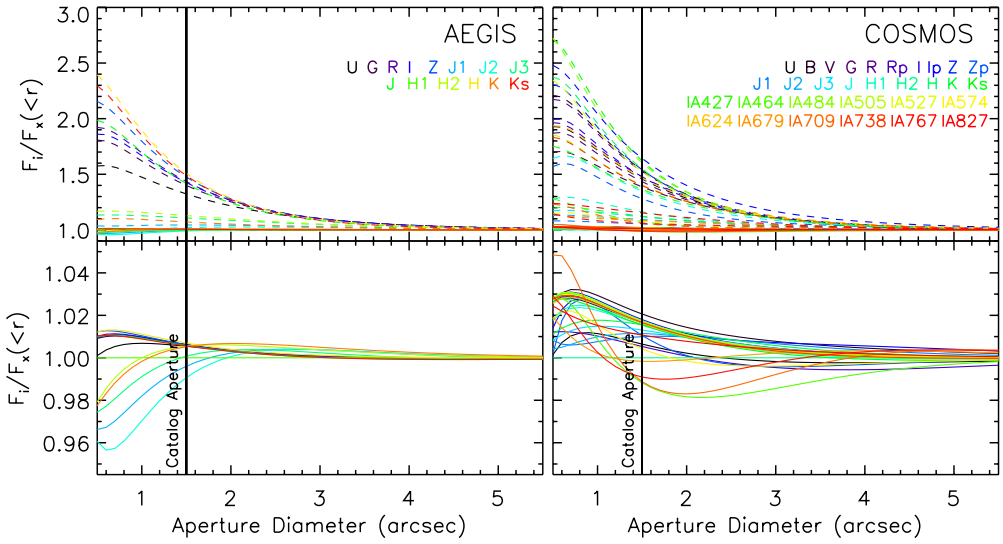

Figure 6. Ratio of the growth curve for all optical-to-NIR bands, F_i, relative to the band with the worst seeing, F_x (where $x = H_1$ in AEGIS and H_2 in COSMOS). The top panel shows the ratio before convolution (dashed lines) and the bottom panel shows after convolution (solid lines). Note the different y-axis scales of the top and bottom panels. The PSF-matched images have accurate colors to <2% for the catalog aperture diameter of 1.″5.

(A color version of this figure is available in the online journal.)

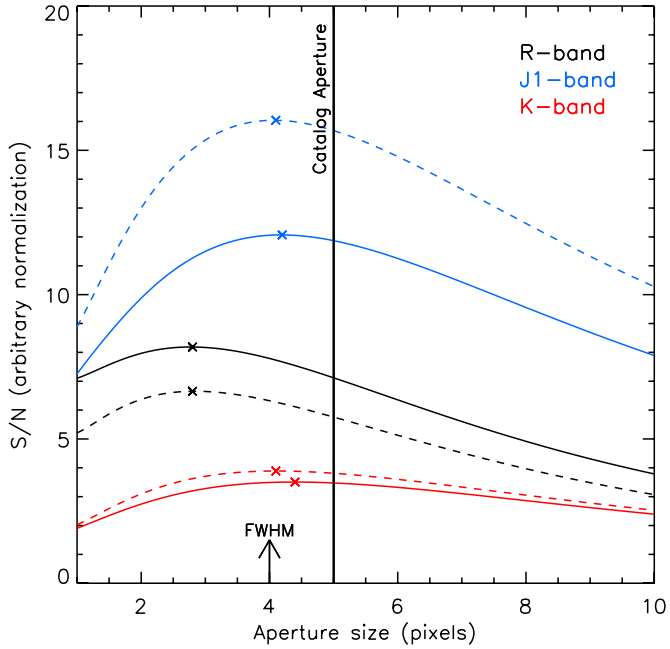

Figure 7. Signal to noise as a function of the aperture size, derived from the ratio of the growth curve and the noise properties for the R- (black), J_1- (blue), and K-band images (red). The solid lines are for the COSMOS field and the dashed lines are for AEGIS, with an "×" marking the peak in S/N. The FWHM of the PSF-matched K-band image is shown with an arrow. We use an aperture diameter of 5 pixels (1.″5) when creating the NMBS catalogs so as to optimize the S/N while remaining larger than the FWHM.

(A color version of this figure is available in the online journal.)

from residual astrometric or PSF matching uncertainties. We note that the K band has a relatively flat slope in S/N, whereas the improvements are most prominent for the J_1 band (shown in Figure 7). There is a 20%–30% loss of S/N when using larger apertures of 2″–3″ in bands blueward of the K band.

The empirical estimate of the background noise $\sigma_{\rm nmad}$ described in Section 3.5 was repeated for all optical and NIR images within the color aperture of 1.″5. From these values, we estimate the flux uncertainties for each object in each band as

$$\sigma^2_{{\rm color},i} = \left(\frac{\sigma_{{\rm nmad},i}}{\sqrt{w_i/w_{{\rm median},i}}}\right)^2 + \frac{F_{{\rm color},i}}{g_i}. \quad (5)$$

The photometric error for each band i is the sum in quadrature of the background uncertainty ($\sigma_{{\rm nmad},i}$; defined in Equation (3)) weighted by the fractional exposure w_i at each object's location relative to the median $w_{{\rm median},i}$, and the source Poisson noise F_i/g_i for each band, with the former dominating the noise for faint sources and the latter for bright sources. F_i is the flux of the object in ADU within a 1.″5 aperture and g_i is the total effective gain. Note that these are the uncertainties of the aperture fluxes, not the total fluxes. The uncertainty in the total fluxes listed in the catalogs is

$$\sigma_{{\rm total},i} = \sigma_{{\rm color},i} \times \frac{K_{\rm total}}{K_{\rm color}}. \quad (6)$$

The K-band total magnitude is calculated from the SExtractor AUTO photometry (see Equation (9)), with an uncertainty calculated as

$$\sigma^2_{K_{\rm tot}} = \left(\frac{\sigma_1 \alpha \left(\pi R^2_{\rm Kron}\right)^{\frac{\beta}{2}}}{\sqrt{w_K/w_{{\rm median},K}}}\right)^2 + \frac{K_{\rm AUTO}}{g_K}, \quad (7)$$

where $R_{\rm Kron}$ is the circularized Kron radius (Kron 1980) and σ_1, α, and β are defined in Equation (3), weighted by the fractional exposure time. The circularized Kron radius is calculated from the semimajor and semiminor axes as $R_{\rm Kron} = \sqrt{\rm A\_IMAGE \times B\_IMAGE \times KRON\_RADIUS^2}$, using the output SExtractor parameters. The following equation can be used to determine the full error in the total magnitude for a single band in isolation, including systematics:

$$\sigma^2_{{\rm full},i} = \sigma^2_{{\rm total},i} + \sigma^2_{K_{\rm tot}} - \sigma^2_{{\rm total},K}. \quad (8)$$

The derivation of the uncertainties for the UV and mid-IR data is described in Sections 4.3 and 4.4.

4.2. Source Detection

The sources are detected in a noise-equalized K-band image using SExtractor in dual-image mode, where the aperture photometry is simultaneously measured on the PSF-matched $u - K$ images. In both fields, the K-band detection image is the unsmoothed (pre-PSF matching) NEWFIRM K-band image multiplied by the square root of the weight map (based on fractional exposure time per pixel). The input SExtractor parameters were optimized so as to find all faint objects while limiting the number of spurious detections. The optimal setting for the minimum number of pixels above the threshold to trigger a detection was 5 pixels, with a detection threshold of 1.2σ and 32 deblending sub-thresholds. We use a Gaussian filter for the detections with an FWHM of 4 pixels, first performing a global background subtraction in all optical–NIR images with a background mesh size of 32 pixels and a smoothing filter of 3 pixels. We note that we used a minimum Kron radius of 3 pixels, compared to the default value of 3.5 pixels. A fixed aperture diameter of 1.″5 (5 pixels) was used to enclose a significant fraction of a given object's flux while minimizing uncertainties due to background fluctuations (see Section 4.1, Figure 7).

Total fluxes were determined using the SExtractor AUTO photometry, which uses a flexible elliptical aperture. This aperture contains the majority of the flux for bright objects but may be missing a large fraction of the light for fainter objects. Therefore, an aperture correction is applied to convert the AUTO flux to total flux (see, e.g., Labbé et al. 2003). The K-band total flux is calculated as follows:

$$K_{\rm total} = K_{\rm AUTO} \times \frac{1}{f_{\rm R<AUTO}}, \quad (9)$$

where $K_{\rm AUTO}$ is the AUTO flux and f is the fraction of light enclosed within the K-band growth curve generated during the PSF matching described in Section 4.1 for a circular aperture with the same area as the AUTO aperture. We force a minimum size of the AUTO aperture equal to the size of the color aperture, affecting <0.1% of the sources. The aperture correction to the AUTO fluxes is typically on the order of 5%–10%, extending to higher values for the faint, extended sources. The total flux for each band i is calculated as

$$F_{{\rm total},i} = F_{{\rm color},i} \times \frac{K_{\rm total}}{K_{\rm color}}, \quad (10)$$

where $F_{{\rm color},i}$ is the flux within a color aperture of 1.″5 diameter (see Equation (4)).

4.3. IRAC/MIPS PSF Matching and Photometry

The FWHM of the IRAC and MIPS images are a factor of about two and about five broader, respectively, than the PSF-matched images. Furthermore, the IRAC and MIPS images contain significant non-Gaussian structure that results from point-source diffraction. Smoothing the optical-to-NIR photometry to the IRAC PSF shape would substantially reduce the S/N and cause significant blending issues in the deep optical data in addition to the IRAC/MIPS images.

We use a source-fitting algorithm developed by one of us (I.L.) that is designed for heavily confused images to extract the photometry from the IRAC and MIPS images (see, e.g., Labbé et al. 2006; Wuyts et al. 2007; Marchesini et al. 2009; Williams et al. 2009). As sources that are bright in K are also typically bright in the IRAC images (and to a lesser extent MIPS images), the K band can be used as a high-resolution template to deblend the IRAC/MIPS photometry. The information on position and extent of the sources based on the higher resolution K-band segmentation map is therefore used to model the lower resolution IRAC 3.6–8.0 μm and MIPS 24 μm images. This technique is similar to Laidler et al. (2007), with one important difference. Laidler et al. (2007) use the best-fit fluxes to calculate flux ratios (colors) directly, whereas our method adds back in the residuals of the fit before performing aperture photometry.

Each source is extracted separately from the K-band image and, under the assumption of negligible morphological K-corrections, convolved to the IRAC/MIPS resolution using local kernel coefficients. The convolution kernels are constructed using bright, isolated, and unsaturated sources in the K and IRAC/MIPS bands, derived by fitting a series of Gaussian-weighted Hermite functions to the Fourier transform of the sources. Outlying or poorly fit kernels are rejected and a smoothed 2D map of the kernel coefficients is stored. All sources in each IRAC/MIPS image are fit simultaneously, with the flux left as a free parameter. The modeled light of neighboring objects is subtracted, thereby leaving a clean IRAC/MIPS image to perform aperture photometry in fixed 3″ apertures for IRAC and 6″ apertures for MIPS. For an illustration of this technique, see Figure 1 in Wuyts et al. (2007).

In order to compute a consistent K-IRAC color, we measure the flux of the objects on a cleaned K-band image convolved to the IRAC resolution within the same aperture to correct the photometry for flux that falls outside of the aperture due to the large PSF size. We then scale the photometry to total fluxes by measuring the ratio of the total K-band flux to the convolved K-band flux within a 3″ aperture for each object:

$$F_{\rm IRAC,catalog} = F_{\rm IRAC,cleaned}(3'') \times \frac{K_{\rm total}}{K_{\rm conv}(3'')}, \quad (11)$$

where $F_{\rm IRAC,cleaned}$ is the flux of the object measured with the modeled light of the neighbors removed, $K_{\rm conv}$ is the flux of the object measured in the K-band image after smoothing it to the IRAC resolution, and $K_{\rm total}$ is the total K-band flux. The $F_{\rm IRAC}$ catalog flux is the total flux that would have been measured in a 1.″5 aperture with an aperture correction if IRAC had the same PSF as the other data.

The uncertainties in the measured fluxes are derived from the residual contamination of the subtracted neighbors. The normalized convolved K-band image of each neighboring source is scaled by the formal 1σ error in the fitted flux as computed from the covariance matrix produced by least-squares minimization. By performing aperture photometry on the image of the residual neighbor contamination, we get the error corresponding to the source flux measured within an aperture of the same size.

The catalog includes the 24 μm flux within fixed 6″ apertures and total fluxes. To measure the total 24 μm flux, we create a MIPS growth curve from several bright, isolated, and unsaturated point sources within each field. These square postage stamps are 12.″6 on a side, and we derive an aperture correction from 6″ to 12.″6 of a factor of 2.8. To convert to total flux, we include an additional aperture correction for the 17% of the flux that falls outside 13″.[20]

4.4. GALEX PSF Matching and Photometry

The *GALEX* FUV band (1350–1750 Å) and NUV band (1750–2800 Å) have 4.″5–6″ resolution (FWHM), roughly

[20] http://ssc.spitzer.caltech.edu/mips/mipsinstrumenthandbook/

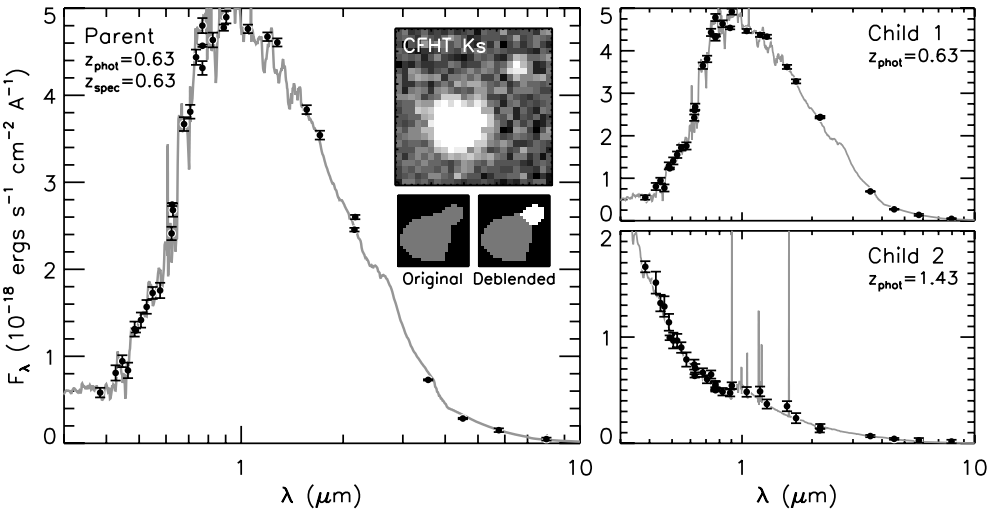

Figure 8. Example of the SED of a galaxy that is blended in the original catalog (left) compared to the SEDs of the deblended children (right). The inset panel shows the CFHT K_S-band image with the original and deblended segmentation maps below. The SEDs of the two children are very different. The photometric redshift of the first child is usually very similar to that of the parent.

∼4–5 times broader than the PSF-matched optical-to-NIR photometry. The same method described in Section 4.3 is used to extract the *GALEX* photometry. In this case, however, the higher resolution prior is the CFHT *u*-band image.

As the *u* band contains many blue galaxies not in the *K*-band detection image, a new segmentation map was generated with SExtractor for the *u* band and matched to the *K*-selected catalog. This allows for all of the objects within the field of view to be modeled to clean the *GALEX* images for aperture photometry, regardless of whether these objects are in the NMBS *K*-selected catalog.

Following Section 4.3, we measure an aperture correction from the flux of the objects on the cleaned *u*-band image convolved to the *GALEX* resolution in order to compute a consistent *GALEX u* color. We then scale the photometry to the same color apertures used for the optical-to-NIR photometry by measuring the ratio of the convolved *u*-band flux within a 6″ aperture and our catalog aperture size for each object, analogous to Equation (11).

4.5. Deblending

A significant fraction of the objects detected by SExtractor are actually blended objects, although classified as single objects. Although SExtractor implements a deblending algorithm, there is no set of parameters that will enable the splitting of close pairs while also detecting faint objects, which requires presmoothing. Deblending the photometry is particularly important when studying the most luminous galaxies; the fraction of sources that are deblended increases from ∼10% at $K = 22$ mag to ∼40% at $K = 20$ mag, reaching as high as ∼80% of sources with $K = 18$ mag. In this section, we describe the method used to deblend the photometry of the single "parent" object into its constituent "children," based on the technique described by Lupton et al. (2001).

The deblending is done using the WIRDS K_S-band image (0.″7 seeing) in COSMOS and a combination of the WIRDS K_S-band image (0.″7 seeing) where the exposure is greater than 30% of the maximum and the non-PSF-matched *K*-band image in AEGIS (1.″1) in the remaining area. Using this criterion, roughly half of the AEGIS deblending image is from the higher resolution WIRDS data. Peaks are found after applying a difference of Gaussian bandpass filter that preserves scales similar to the seeing size. Object templates are created by comparing pairs of pixels symmetrically around the peak and replacing both by the lower value. False peaks are rejected if the total template S/N < 3 or if the template peak value is less than two times the combined pixel value of all other templates at that location. Finally, we solve for the template weights by a linear fit of the templates to the image, and then assign flux to every pixel of each child according to the relative contribution of the weighted templates. The segmentation map is updated, assigning each pixel to the child with the largest contribution.

Using the peaks previously found in the high-resolution image, the deblending procedure is repeated for each $u - K$ background-subtracted, PSF-matched image. Aperture photometry in 1.″5 color apertures is then performed on the "deblended" children. Total fluxes are computed by dividing the parent total flux according to the aperture flux ratio of the children, thus conserving the total flux of the parent. The IRAC and MIPS photometry of the children is remeasured using the method described in Section 4.3, but now using the new deblended segmentation map and the positions of the children. Due to the large PSF size of the *GALEX* data and the lack of a deblended *u*-band segmentation map, no attempt was made to deblend the NUV and FUV data.

2186 and 3017 objects in the original catalogs were split into 5019 and 6803 children in AEGIS and COSMOS, respectively. New identification numbers of the children start at ID = 30000. On average, the difference between the total *K*-band flux of the brightest child relative to the parent increases with redshift, with a median difference of 0.1 mag at $z \sim 0.5$ and 0.3–0.4 mag at $z > 1.5$.

Figure 8 shows an example of an object that has been deblended with the above algorithm. Although classified as a single object by SExtractor, there is clearly a faint neighbor. The deblending technique recovers a well-described SED of the faint neighbor, with a notably different shape and photometric redshift compared to the brighter galaxy. It is worthwhile to note that, in the case of a fainter neighboring object (e.g., child 2 in Figure 8), the photometric redshift of the brighter object (child 1) is generally not significantly different from the parent, even though the children can have vastly different spectral shapes and photometric redshifts.

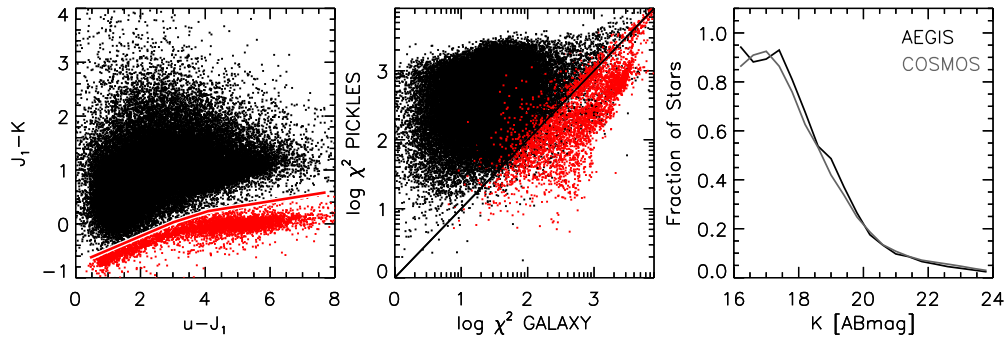

Figure 9. Objects are classified as stars (red) from their $u - J_1$ and $J_1 - K$ colors in the left panel. These same objects also have SEDs that tend to be better fit by the stellar templates than the galaxy templates (middle panel). All objects in both catalogs are shown, with no quality cuts applied. The fraction of stars relative to the total number of objects as a function of K-band magnitude for both fields is shown in the right panel.

(A color version of this figure is available in the online journal.)

4.6. Star Classification

It is important to distinguish between galaxies and objects that are likely stars in the photometric catalog. Stellar SEDs have a characteristically steep rise and fall in their spectra, resulting in a tight stellar sequence in their $u - J$ and $J - K$ colors relative to the colors of galaxies. This is shown in Figure 9: stars (red) form a distinctive sequence with blue $J - K$ colors for a wide range of $u - J$ colors as compared to galaxies (black).

Stars are flagged based on the $u - J_1$ and $J_1 - K$ colors of all objects, where any objects satisfying the following limits (corresponding to the red line in Figure 9) will be classified as a star:

$$\begin{aligned} J_1 - K &< -0.74 + 0.26(u - J_1) \quad [u - J_1 < 3] \\ J_1 - K &< -0.55 + 0.19(u - J_1) \quad [3 < u - J_1 < 4] \\ J_1 - K &< -0.16 + 0.10(u - J_1) \quad [u - J_1 > 4]. \end{aligned} \tag{12}$$

The middle panel in Figure 9 shows the χ^2 values for the stars (red) and galaxies (black) when fit with the Pickles (1998) stellar template library compared to the default set of EAZY galaxy templates. The vast majority of objects that are classified as stars through their $u - J$ and $J_1 - K$ colors are better fit with the stellar templates. The fraction of objects that are classified as stars relative to the total number of objects as a function of K-band magnitude is shown in the right panel of Figure 9 for both fields. Almost all objects brighter than $K \sim 16$ mag are stars.

We have compared our star classification to the COSMOS *HST* Advanced Camera for Surveys catalog,[21] matching objects within a radius of 1″. We find that > 90% of the objects classified as stars using the higher resolution I-band data also fall within our $u - J_1$ and $J_1 - K$ color selection limit in Equation (13). The star classification method seems robust, although we note that there may be a small fraction of objects (<10% of stars and <1% of galaxies) that are misclassified, especially close to the detection limit.

4.7. Catalog Format

The final K-selected catalog consists of 24,739 and 27,520 objects detected by SExtractor in the AEGIS and COSMOS mosaics, with a total of 27,572 and 31,306 objects in the deblended catalogs. Photometry in the FUV through the MIPS 24 μm band is included, with additional optical broadband and medium-band photometry in the COSMOS field. The catalog fluxes can be converted into total magnitudes as follows:

$$m = -2.5 \log F + 25, \tag{13}$$

where F is the total flux density of the object with a magnitude m normalized to a zero point of 25 in the AB system, corresponding to a flux density of 3.631×10^{-30} erg s^{-1} Hz^{-1} cm^{-2} (or 0.3631 μJy). To convert from total magnitudes to the color aperture magnitude, the fluxes and errors should be multiplied by the ratio of the K-band aperture flux (`Kaper`) to the total K-band flux. A description of the columns included in the version 5.1 catalogs can be found in Table 2.

A standard selection of galaxies can be obtained by selecting `use` = 1 for either the original SExtractor catalog or the deblended catalog, which is equivalent to `wmin` >0.3 and `star_flag` = 0. An additional cut on the S/N of the galaxies may be optimal.

4.8. Completeness

We estimate the (point-source) completeness of our catalogs as a function of magnitude by attempting to recover simulated sources within the K-band noise-equalized detection images. The simulated point sources were generated from the K-band empirical PSF described in Section 4.1, before smoothing. The empirical PSF is scaled to the desired flux level and inserted at random locations within the entire image. We then run SExtractor using the same settings described in Section 4.2, determining the fraction of recovered sources as a function of input K-band total magnitude. Figure 10 shows the resulting completeness curves from this analysis. The completeness curves qualitatively agree with the raw number counts of galaxies within the fields shown in the inset plot.

A fraction of the simulated point sources will fall on or close to other objects and these blended objects may not be properly handled by SExtractor. We have also repeated the simulations by inserting the point sources in locations that do not overlap with the segmentation map, thereby "masking" the original detected sources (dotted lines in Figure 10). We include the 90% and 50% completeness limits for both the masked and unmasked simulations in Table 3. We note that about 10% of the objects are blended within the original catalogs produced by SExtractor, as determined by the additional deblending algorithm described in Section 4.5. When using the deblended catalogs, these completeness limits may therefore be slightly conservative. As the NMBS K-band fields are not overly crowded, the completeness limits for both simulations are similar.

[21] http://irsa.ipac.caltech.edu/data/COSMOS/datasets.html

Table 2
Summary of Photometric Catalog Contents

Column No.	Column Title	Description
1	id	Object identifier, beginning from 1
2,3	x, y	*x*- and *y*-image coordinates
4,5	ra, dec	Right ascension and declination (J2000.0; decimal degrees)
6,7	Kaper, eKaper	Color aperture *K*-band flux and error
8–82 (8–67)[a]	X, eX, wX	Total flux, error, and weight in each filter
83–106	X, eX	Total flux and error of the COSMOS optical medium bands
107 (68)	ftot24um_uJy	Total MIPS 24 μm flux (μJy)
108, 109 (69, 70)	f24um_uJy, e24um_uJy	Aperture flux within 6″ and error of MIPS 24 μm (μJy)
110 (71)	w24um	Weight of MIPS 24 μm
111 (72)	wmin	Weight of $u - K$ band with minimum exposure
112 (73)	wmin_irac	Weight of IRAC band with minimum exposure
113 (74)	z_spec	Spectroscopic redshift, if available (matched within 1″ radius)
114 (75)	star_flag	Star flag (1 = Star, 0 = Galaxy)
115, 116 (76, 77)	ap_col, ap_tot	Size of the color aperture and total aperture in arcseconds
117 (78)	totcor	Aperture correction applied to the *K*-band AUTO flux to convert to total flux
118, 119 (79, 80)	K_ellip, K_theta_J2000	*K*-band ellipticity and position angle from SExtractor
120 (81)	K_R50	*K*-band half-light radius from SExtractor (pixels)
121 (82)	K_class_star	*K*-band SExtractor parameter measuring stellarity of object
122, 123 (83, 84)	K_flags, UH2_flags	*K*-band detection flag and maximum detection flag from $u - H_2$ from SExtractor
124 (85)	Near_Star	Signifies object is near a bright star and photometry may be affected
125–130 (86–91)	X_contam	Ratio of the IRAC/*GALEX* flux in neighboring objects removed to the "cleaned" flux
131 (92)	contam_flag	IRAC/*GALEX* contamination ratio >50% in any band (1 = >50% in $\geqslant$1 band, 0 = OK)
132, 133 (93, 94)	nchild, id_parent	Number of children from deblended catalog (−1 if child) and ID of parent (−1 if parent)
134 (95)	use	Standard selection of galaxies for either the deblended or the original catalogs (use = 1)

Note. [a] AEGIS column numbers are in parentheses, as the COSMOS catalog contains additional bands.

Table 3
Point-source Completeness Limits

Field	Masking Sources		Entire Image	
	90% Limit[a]	50% Limit	90% Limit	50% Limit
AEGIS	23.2	23.7	22.5	23.6
COSMOS	23.2	23.6	22.1	23.4

Note. [a] All magnitudes are given in the AB system.

4.9. Number Counts

Figure 11 shows the surface density of galaxies as a function of magnitude in the NMBS fields compared to other galaxy number-count analyses drawn from the literature. Objects that are classified as stars (see Section 4.6) have been excluded from this calculation. The number counts are calculated in 0.4 mag bins using objects within the image area with >30% of the total *K*-band exposure time (∼0.21 deg^2 in both fields).

The number counts of the NMBS fields have been corrected for incompleteness using the simulations without masking, as calculated in Section 4.8. We note that the completeness values only provide a simplistic correction to the surface density of objects, whereas a more sophisticated analysis would account for the difference between measured and intrinsic fluxes of the synthetic sources. Due to the potential biases in the photometry of the faintest sources, we only extend the average number counts to $K \sim 22.7$, where the completeness correction begins to become significant (Figure 10).

The number counts of the NMBS fields agree with the large compilation of data sets within the scatter due to field-to-field variations. We note that the COSMOS field appears to have a relatively high density of objects at $K < 18$ mag. We refer the reader to Wake et al. (2011) for a detailed analysis of the relative densities and galaxy clustering in the NMBS fields.

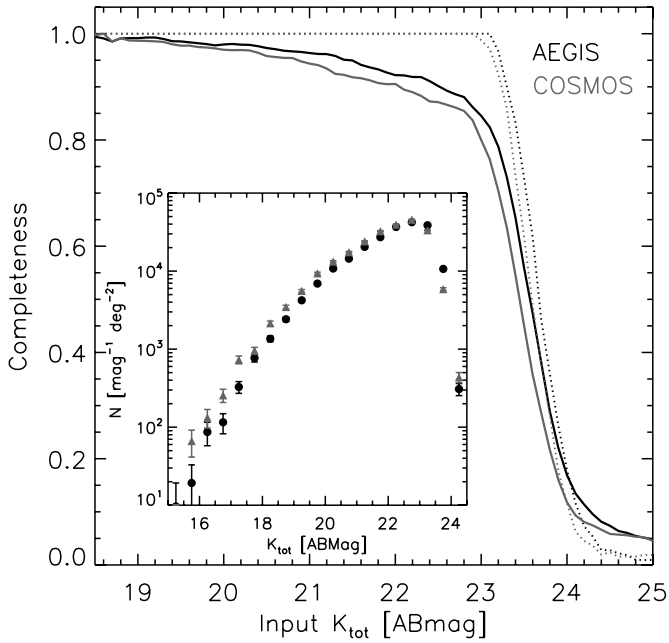

Figure 10. *K*-band completeness curves; the completeness is defined as the fraction of simulated point sources that were recovered as a function of the total *K*-band magnitude of the simulated source. The point sources were inserted at random locations across the entire image where the exposure map was greater than half the maximum exposure, with no masking (solid lines) and detected sources masked (dotted lines). The inset plot shows the raw number counts of galaxies within the two NMBS fields shown with Poisson error bars, with no corrections for incompleteness.

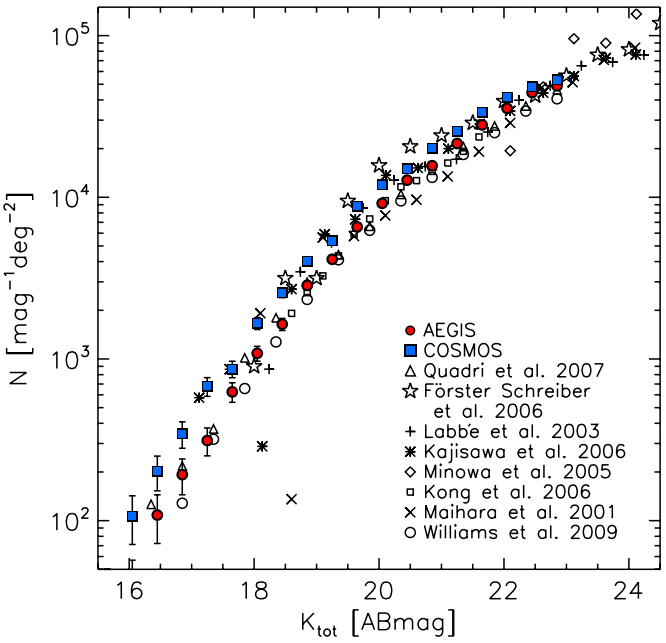

Figure 11. Average galaxy number counts from the two NMBS fields, along with a compilation of results from the literature. Poisson error bars are shown for the NMBS fields; the other fields have comparable uncertainties. The NMBS fields have been corrected for incompleteness, but only points where this correction is $\lesssim$20% are shown.

(A color version of this figure is available in the online journal.)

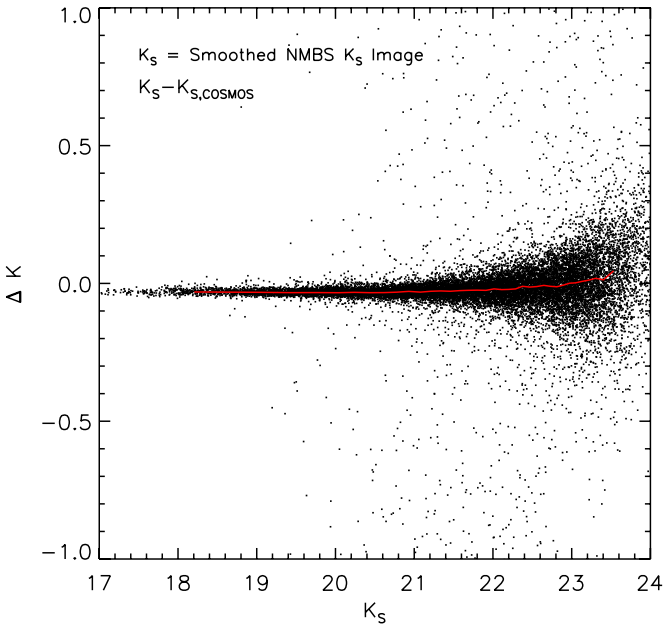

Figure 12. Difference in *K*-band magnitude between the NMBS K_S image smoothed with a Gaussian to 1.″5 seeing and the COSMOS catalog magnitude within 3″ apertures (black points). The running median (red) indicates that there are no significant systematic zero-point offsets between the two catalogs.

(A color version of this figure is available in the online journal.)

4.10. Comparison to Other Photometric Catalogs

We have compared our *K*- and K_S-band flux measurements to the COSMOS survey catalog (Capak et al. 2008; Ilbert et al. 2009).[22] The COSMOS catalog is *I*-selected and quotes fluxes within a 3″ aperture with an aperture correction provided to convert to AUTO fluxes (see Capak et al. 2007, 2008). The K_S-band data in the COSMOS catalog is derived from an earlier CFHT K_S image taken during the 2004–2005 observing season, whereas we include the publicly available K_S image with photometry from the 2005–2007 observing seasons for this analysis. As the COSMOS K_S image used to make the publicly available COSMOS catalog has 1.″5 seeing (compared to ∼0.″8 seeing in the image version used in the NMBS catalogs), we smooth our K_S image with a Gaussian kernel to 1.″5 and compare the fluxes between the catalogs.

Figure 12 shows the difference in K_S-band magnitude between the smoothed NMBS K_S image and the magnitude quoted within a 3″ aperture in the COSMOS catalog (black points) for all objects. The results indicate that there are no significant systematic zero-point offsets between the NMBS and COSMOS catalogs.

We have also compared the *GALEX* and IRAC flux measurements to publicly available catalogs, finding excellent agreement. We exclude comparisons to catalogs where it is unclear how aperture corrections are applied as the interpretation is difficult, but note that there were not any large systematic offsets. The COSMOS *GALEX* NUV and FUV catalog fluxes within 3″ apertures agree within ∼0.05 mag with the public catalogs available through the Multimission Archive.[23] The AEGIS NMBS IRAC photometry within 3.″5 apertures has a median difference of <0.03 mag for all channels when compared to the EGS catalog.[24] Finally, we have also compared the MIPS total fluxes in COSMOS to the S-COSMOS GO3 catalog, finding excellent agreement with a median offset of <1%. In general, the photometry of the NMBS catalogs agrees well with all publicly available catalogs within the fields.

5. PHOTOMETRIC REDSHIFTS

Photometric redshifts and rest-frame colors were derived using the EAZY code[25] (Brammer et al. 2008), which fits linear combinations of seven templates to the broadband and medium-band SEDs. A *K*-band apparent magnitude prior and systematic errors due to template mismatch are taken into account. The optimized template set used for the EAZY photometric redshift code contains seven templates, which is large enough to span a broad range of galaxy colors while minimizing color and redshift degeneracies. The default template set is described in detail in Brammer et al. (2008); this set includes five templates generated based on the PÉGASE population synthesis models (Fioc & Rocca-Volmerange 1999) and calibrated with synthetic photometry from semi-analytic models as well as an additional young and dusty template added to compensate for the lack of extremely dusty galaxies in semi-analytic models. We include an additional template for an old, red galaxy from the Maraston (2005) models, with a Kroupa (2001) initial mass function and solar metallicity for a stellar population that has an age of 12.6 Gyr. The choice of template set is important for both the photometric redshifts and rest-frame colors (see Appendix C of Whitaker et al. 2010 for $\log M_{\odot} > 11$). We adopt `z_peak` as the photometric redshift (except where otherwise noted), which finds discrete peaks in the redshift probability function and returns the peak with the largest integrated probability.

[22] http://irsa.ipac.caltech.edu/data/COSMOS/tables/redshift/
[23] http://archive.stsci.edu/prepds/cosmos/galexdatalist.html
[24] http://www.cfa.harvard.edu/irac/egs/
[25] http://www.astro.yale.edu/eazy/

Table 4
Zero-point Offsets

Filter	AEGIS[a]	COSMOS
U	−0.22	−0.23
B	...	−0.07
G	−0.01	−0.02
V	...	0.12
R	−0.01	−0.03
Rp	...	0.03
I	0.03	0.00
Ip	...	−0.34
Z	0.05	−0.01
Zp	...	0.11
J	−0.03	−0.08
J_1	−0.00	−0.01
J_2	−0.00	−0.01
J_3	−0.01	−0.02
H	−0.03	−0.02
H_1	0.01	−0.01
H_2	−0.01	−0.03
K	0.00	0.00
K_S	0.04	−0.05
$IA427$	...	−0.11
$IA464$	...	−0.16
$IA484$	...	−0.11
$IA505$	...	−0.02
$IA527$	...	−0.06
$IA574$	...	−0.12
$IA624$	...	0.04
$IA679$	...	0.24
$IA709$	...	0.15
$IA738$	...	−0.04
$IA767$	...	0.07
$IA827$	...	−0.12

Note. [a]All zero-point offsets are in magnitudes, defined as $ZP_{EAZY} = ZP_{nominal}$ + offset.

Uncertainties in the photometric zero points of the numerous photometric bands can lead to systematic shifts in the observed colors, and thus the redshift estimates, of the sample. We compute offsets of the photometric zero points by fitting the EAZY templates to the full optical–NIR SEDs of objects with spectroscopic redshift measurements, with the fit redshift fixed to the spectroscopic value. The offsets are computed iteratively by minimizing the de-redshifted fit residuals, which allows the separation of zero-point errors from systematic effects associated with the choice of templates, since a given rest-frame wavelength is sampled by different observed bands at different redshifts. The zero-point offsets are listed in Table 4 and included in the catalog.

While the majority of the bands require only small offsets ($\lesssim$0.02 mag), some of the optical bands require offsets of as much as 0.3 mag (see also Table 1 in Ilbert et al. 2009). We have verified that this technique reliably recovers artificial zero-point errors of 0.02–0.3 mag added to the observed photometry. The CFHTLS u-band zero point is uncertain and known to have issues; a direct comparison between the CFHT u band and Sloan Digital Sky Survey suggests a difference of 0.1 mag (Erben et al. 2009). The derived u-band zero-point offset may be partly influenced by the choice of template set. As a result, it is difficult to separate true zero-point problems from template mismatch. Furthermore, the u-band zero point is not well constrained as it is not bracketed by other filters—except the *GALEX* filters, which have their own known zero-point uncertainties up to ∼0.3 mag (e.g., Ilbert et al. 2009).

We find the photometric redshifts in COSMOS to be in excellent agreement with the magnitude-limited I-band $I_{AB} < 22.5$ spectroscopic sample of redshifts from the zCOSMOS survey (Lilly et al. 2007), with $\sigma_z/(1+z) = 0.008$ for 1509 galaxies (right panel, Figure 13), where $\sigma_z/(1+z)$ is the normalized median absolute deviation, or $\sigma_{NMAD} = 1.48 \times MAD$. These values are quoted only for $z_{spec} < 1$, as there are currently very few spectroscopic redshifts publicly available in the COSMOS field beyond this redshift. We also find excellent agreement between the photometric and spectroscopic redshifts for a larger sample of 2525 objects at $z_{spec} < 1.5$ in AEGIS selected to a R-band limit of $R_{AB} < 24.1$ from the Deep Extragalactic Evolutionary Probe 2 survey (Davis et al. 2003) with $\sigma_z/(1+z) = 0.017$ (left panel, Figure 13). Both fields have very few catastrophic failures, with only ∼5% > 5σ outliers, defined such that $|z_{phot} - z_{spec}|/(1+z_{spec}) < 5\sigma_{NMAD}$. Spectroscopic redshifts are available for 117 Lyman break galaxies (LBGs) at $z \sim 3$ within the AEGIS field from Steidel et al. (2003), for which we find $\sigma_z/(1+z) = 0.044$, with 10% > 5σ outliers. These relatively high photometric redshift uncertainties for LBGs are well known (Reddy et al. 2008) and caused by the fact that LBGs tend to be faint in the rest-frame optical (observer's NIR) and their spectra have relatively weak Balmer/4000 Å breaks. We also note that there is excellent agreement between the NIR medium-band photometric redshifts and the Gemini/GNIRS redshifts from Kriek et al. (2006), with a biweight scatter in $|z_{phot} - z_{spec}|/(1 + z_{spec})$ of only 0.010, albeit only for four galaxies (see van Dokkum et al. 2009). The photometric redshift accuracies range from $\sigma_z/(1+z) \sim 1\%$ for galaxies with stronger Balmer/4000 Å breaks to $\sigma_z/(1+z) \sim 5\%$ for galaxies with less-defined breaks from the spectroscopic redshift sample. Recently, Kriek et al. (2011) find that the photometric redshift errors must be $\lesssim$2% given the shape of the observed Hα emission line, as built from composite SEDs of the medium-band photometry itself.

In an effort to fill in the void of spectroscopic redshifts for K-selected galaxies above $z \sim 1$, follow-up spectroscopy for several massive galaxies at $z \sim 1.5$–3.5 has been pursued. Preliminary spectroscopic redshifts are in excellent agreement with the NMBS photometric redshifts (see R. Bezanson et al. 2011, in preparation and I. Labbé et al. 2011, in preparation). We include the currently available preliminary spectroscopic redshifts in the right panel of Figure 13.

In Figure 14, we see that the scatter in the photometric–spectroscopic redshift comparison is relatively uniform as a function of the K-band magnitude. There is a larger scatter among the high-redshift LBGs (blue), which is not surprising given the spectral shapes and faint K-band magnitudes of these galaxies.

The photometric redshift distributions of both fields are shown in Figure 15, using the EAZY `z_mc` redshift. This redshift value is drawn randomly from the redshift probability distribution, where the distribution of these redshifts for a given sample of objects very closely follows the summed probability distribution of those same objects (Wittman 2009). The fields have independent spikes in redshift space, indicating the presence of known overdensities (see, e.g., Olsen et al. 2007). The overdensities in COSMOS at $z \lesssim 1$ are more prominent due to the addition of the 12 medium-band optical filters and may also be partly due to the relative variance in the size of the structures from field to field. Additionally, we show the distribution of apparent K-band magnitude as a function of

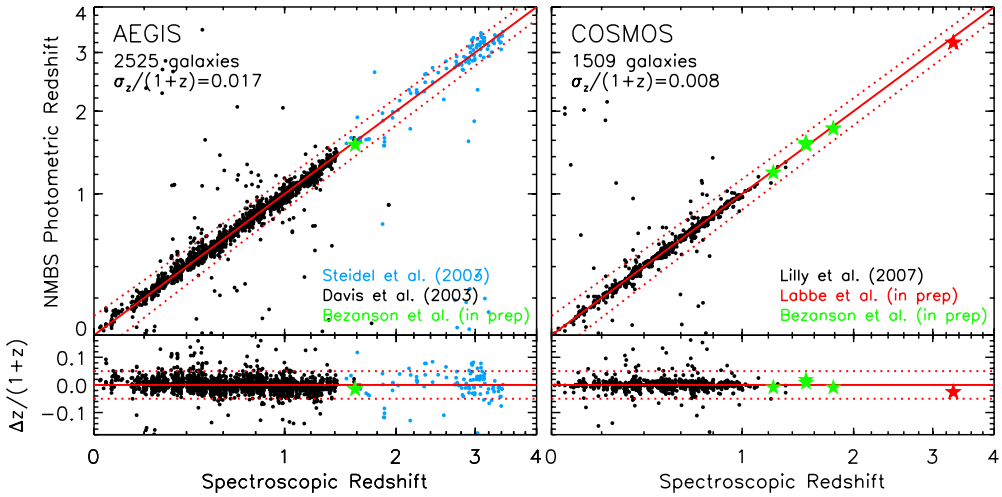

Figure 13. Comparison between the NMBS photometric redshifts of the deblended catalog and spectroscopic redshifts from the DEEP-2 sample (Davis et al. 2003) and a smaller sample of high-redshift LBGs (Steidel et al. 2003; left panel), and the zCOSMOS survey (Lilly et al. 2007; right panel). A few preliminary spectroscopic redshifts from R. Bezanson et al. (2011, in preparation) and I. Labbé (2011, in preparation) are included. For reference, the red dashed lines are for $z_{\rm phot} = z_{\rm spec} \pm 0.05(1 + z_{\rm spec})$. The correspondence between the photometric and spectroscopic redshifts is generally very good.

(A color version of this figure is available in the online journal.)

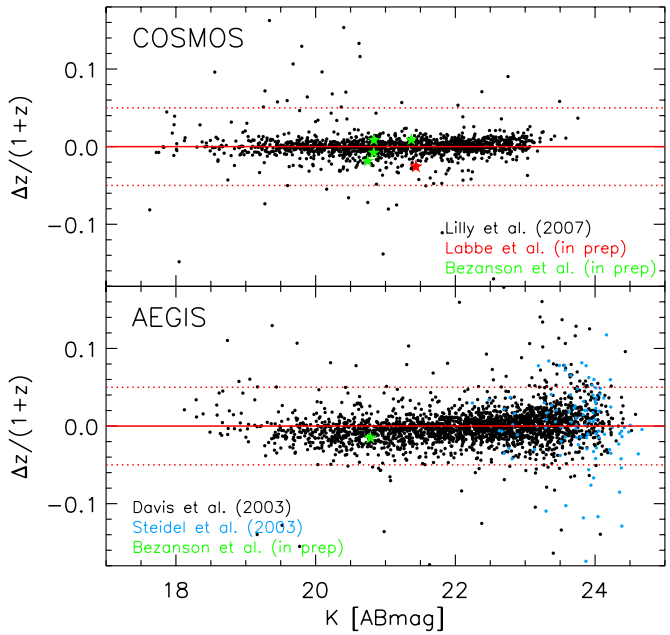

Figure 14. Scatter in the photometric and spectroscopic redshifts of the deblended catalogs is relatively uniform as a function of the K-band magnitude, with a larger scatter among the faint, high-redshift LBGs (blue). The spectroscopic redshifts are from the zCOSMOS survey (Lilly et al. 2007; top panel) and the DEEP-2 sample (Davis et al. 2003) with a small sample of high-redshift LBGs (Steidel et al. 2003; bottom panel). We also include preliminary spectroscopic redshifts from R. Bezanson et al. (2011, in preparation) and I. Labbé (2011, in preparation). The red dashed lines are for $z_{\rm phot} = z_{\rm spec} \pm 0.05(1+z_{\rm spec})$.

(A color version of this figure is available in the online journal.)

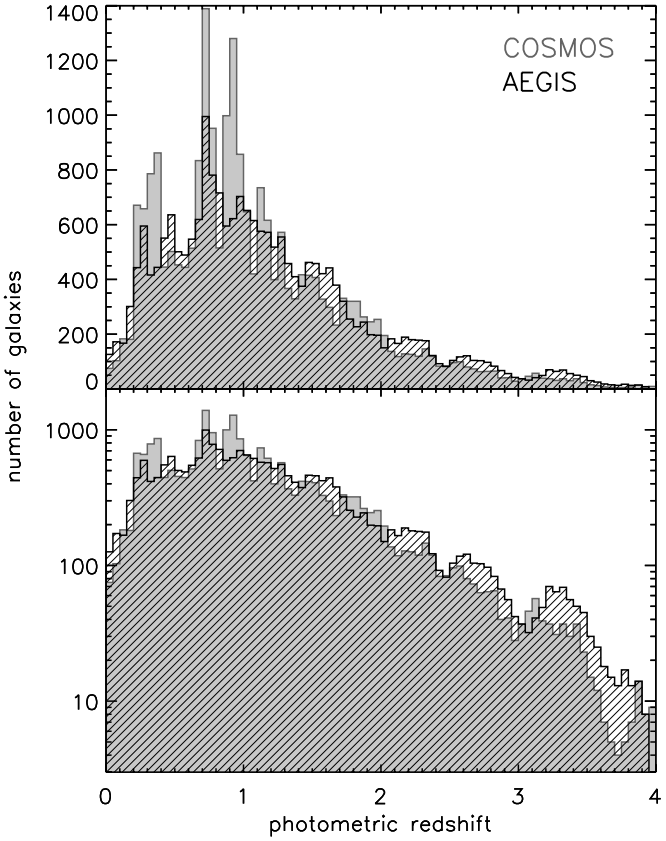

Figure 15. Linear (top) and logarithmic (bottom) photometric redshift distributions of AEGIS (black) and COSMOS (gray), using the EAZY `z_mc` redshift (see definition from Wittman 2009). We use the standard selection of galaxies (use = 1) with $K_{\rm tot}$ greater than the 50% completeness limits from the unmasked simulations (23.6 and 23.4 mag in AEGIS and COSMOS). The spikes coincide with known overdensities. There are 12,632 galaxies at $z > 1.5$ shown here.

photometric redshift (now `z_peak`, as throughout the rest of the paper) of all galaxies in the NMBS fields in Figure 16.

6. EVIDENCE FOR QUIESCENT GALAXIES TO $z \sim 3$

Galaxies within the local universe lie in two distinct classes: actively star-forming galaxies and "quiescent" galaxies with evolved stellar populations and little ongoing star formation. These populations show strong bimodal behavior in their colors (Kauffmann et al. 2003; Baldry et al. 2004), where the red, quiescent galaxies have a more luminous characteristic magnitude and a shallower faint-end slope of the luminosity and mass functions compared to those of blue galaxies.

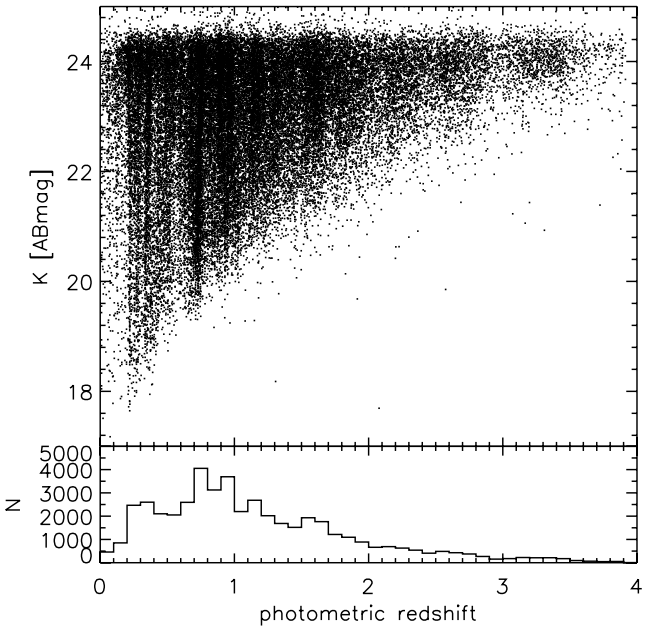

Figure 16. Distribution of apparent *K*-band magnitude as a function of the photometric redshift (`z_peak`) for all galaxies in the NMBS fields (top) and the number of galaxies as a function of their photometric redshift (bottom).

Quiescent galaxies fall into a distinct "red sequence" in color–magnitude diagrams at low redshift. However, at high redshifts dusty, star-forming galaxies can have similarly red $U-V$ colors, "contaminating" the red sequence. Including the $V-J$ rest-frame color can help separate out the dusty, star-forming galaxies (Labbé et al. 2007; Wuyts et al. 2007; Williams et al. 2009; Ilbert et al. 2009). At fixed $U-V$, passively evolving galaxies have blue $V-J$ colors, whereas dusty galaxies have red $V-J$ colors. The location of the red clump of quiescent galaxies in the *UVJ* plane shifts toward bluer $U-V$ colors toward higher redshift, while the $V-J$ colors remain essentially unchanged. This change in rest-frame color with redshift reflects the intrinsic passive evolution of the stellar population. However, the uncertainties in the rest-frame colors will also increase with redshift, potentially washing out any intrinsic bimodality. These two effects have made detections of the bimodality difficult at high redshift.

This bimodal color sequence has been shown to persist out to $z\sim2$ both photometrically (e.g., Labbé et al. 2005; Daddi et al. 2005; Taylor et al. 2009a; Williams et al. 2009; Whitaker et al. 2010) and spectroscopically (e.g., Giallongo et al. 2005; Franzetti et al. 2007; Cassata et al. 2008; Kriek et al. 2008a). A population of massive, quiescent galaxies at $z\sim2$ is surprising. The ages of the stellar populations of these galaxies are a significant fraction of the age of the universe, which was only a few gigayears at these redshifts. The existence of massive galaxies with strongly suppressed star formation at such high redshifts provides useful constraints on models of galaxy formation (e.g., Baugh 2006). It is unclear at what point in cosmic time this bimodal color sequence emerges, due to limitations governed by the accuracies of the photometric redshifts and rest-frame colors.

The accurate redshifts and rest-frame colors of the NMBS are well suited for studies of the evolution of the bimodal color distribution of galaxies. In Brammer et al. (2009), we selected 25,000 galaxies from the NMBS, showing that the dust-corrected rest-frame $U-V$ color distribution is bimodal out to $z\sim2.5$. Additionally, Whitaker et al. (2010) measured an increase in the intrinsic scatter of the rest-frame $U-V$ colors of massive, quiescent galaxies in the NMBS out to $z\sim2$. This scatter in color arises from the spread in ages of the quiescent galaxies, where we see both quiescent red, old galaxies and quiescent blue, younger (post-starburst) galaxies toward higher redshift. Both of these studies were based on NMBS catalogs from the 2008A and 2008B data alone, whereas here we are using a deeper catalog containing the entire survey data set. Also using the latest NMBS catalog, Marchesini et al. (2010) showed that the most massive galaxies ($>2.5\times10^{11}\,M_{\odot}$) at $3<z<4$ are typically red and faint in the observer's optical with quenched star formation, extending the evidence for quiescent galaxies beyond $z\sim3$ with a sample of 14 very massive galaxies.

Rest-frame $U-V$ and $V-J$ colors are derived by integrating the redshifted rest-frame filter bandpasses from the best-fit EAZY template. We use the *UBV* bandpasses defined by Maíz Apellániz (2006) and the Two Micron All Sky Survey *J* bandpass. This method for determining rest-frame fluxes is similar to that used by the COMBO-17 survey described by Wolf et al. (2003). We find that in most cases this method provides very similar results to the algorithm described by van Dokkum & Franx (1996) and Taylor et al. (2009a), though the direct template fluxes are more robust when narrower, closely spaced filters are used, as is the case here. A more detailed explanation of the rest-frame color algorithm is provided by Brammer et al. (2011). We note that the observed *u* band is used in determining the rest-frame $U-V$ colors for low-redshift galaxies ($z\lesssim0.4$). In order to limit biases, we do not use the zero-point offset, which gives the best template fits in the rest-frame color determinations due to the large uncertainties.

Figure 17 shows the rest-frame $U-V$ versus $V-J$ diagram for the NMBS galaxies, selecting galaxies with an S/N >8 in the *K* band. For the first time, we show the bimodal distribution of star-forming and quiescent galaxies based on their rest-frame colors out to a remarkably high redshift of $z\sim3$. A pronounced "quiescent clump" is visible at red $U-V$ colors above the star-forming sequence out to $z=2.5$, with some evidence of a bimodality at $2.5<z<3.5$. This clump appears to shift to bluer colors at higher redshift. We note that the shape of the red clump of quiescent galaxies at $0<z<0.5$ extends to bluer $U-V$ colors, whereas the analogs of these galaxies appear to be absent at all other redshifts. This effect may be caused by low-mass quiescent galaxies with lower metallicities that are below our *K*-band detection limit at higher redshifts. We also note that the $U-V$, $V-J$ plane would be populated differently in an optically selected survey: there would be more faint, blue galaxies that fall in the lower left corner. The incompleteness of this flux-limited sample leads to an apparent increase in the number of quiescent galaxies relative to blue, star-forming galaxies at the highest redshifts. Using a mass-selected sample of quiescent galaxies, Whitaker et al. (2010) have shown that the fraction of quiescent galaxies falls below 40% at $z>2$.

As stellar population parameters are dependent on the stellar population synthesis models (see, e.g., Wuyts et al. 2007; Muzzin et al. 2009; Conroy et al. 2009, 2010), we adopt the model-independent selection criteria of quiescent galaxies of Williams et al. (2009) based on the rest-frame $U-V$ and $V-J$ colors. We have modified the selection limits of Williams et al. (2009) at $z>1$, with the following adopted diagonal selection criteria:

$$(U-V)>0.88\times(V-J)+0.69\ [z<0.5]$$
$$(U-V)>0.88\times(V-J)+0.59\ [z>0.5]. \quad (14)$$

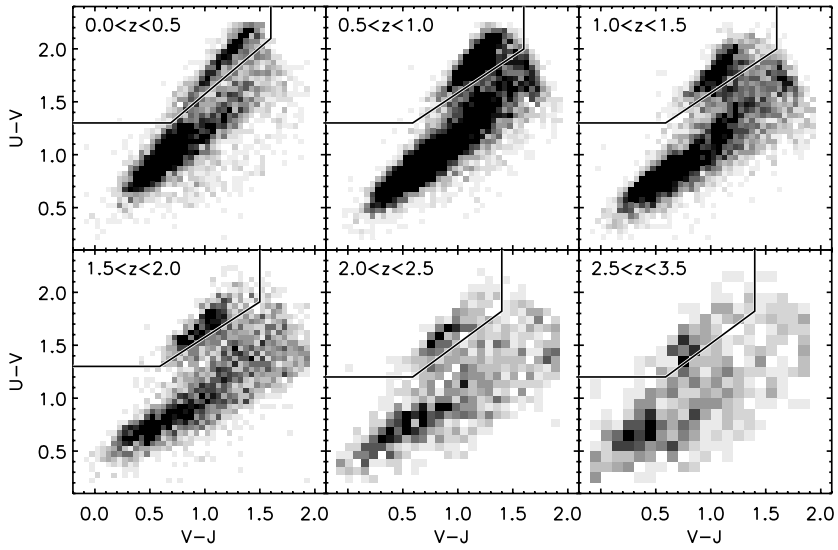

Figure 17. Rest-frame *UVJ* diagram for NMBS galaxies with S/N > 8 in the *K* band out to a redshift of 3.5. The gray scale represents the density of points, with the lines indicating the separation between quiescent "red sequence" galaxies and star-forming galaxies (both blue and red). The quiescent galaxies can be traced to the highest redshift interval $2.5 < z < 3.5$. Apparently, the first quiescent galaxies stopped forming stars by that redshift (see also Marchesini et al. 2010).

Additionally, we modify the limits in $U-V$ and $V-J$ such that

$$\begin{aligned}(U-V) &> 1.3, (V-J) < 1.6\ [0.0 < z < 1.5]\\ (U-V) &> 1.3, (V-J) < 1.5\ [1.5 < z < 2.0]\\ (U-V) &> 1.2, (V-J) < 1.4\ [2.0 < z < 3.5],\end{aligned} \quad (15)$$

where these constraints on the $U-V$ and $V-J$ colors prevent contamination from unobscured and dusty star-forming galaxies, respectively. The clump of quiescent galaxies is separated by only ∼0.3 mag in $U-V$ color from the blue, star-forming sequence at $z \sim 3$. We note that this offset is larger than the typical uncertainties in the rest-frame colors at $z \sim 3$ of <0.1 mag. We speculate that if we were able to resolve enough galaxies at $z \sim 3.5$–4, we might begin to see the epoch where this color bimodality breaks down.

In Figure 18, we demonstrate the quality of the SEDs of quiescent galaxies in the highest redshift bin of Figure 17. The *K*-band S/N of these $z \sim 3$ galaxies ranges from S/N ∼ 35 for the brightest galaxy ($K \sim 22$ mag) down to S/N ∼ 9 for the faintest galaxies ($K \sim 24$ mag). The majority of the galaxies shown in Figure 18 have little to no rest-frame UV emission, indicating little ongoing star formation. We note that the rest-frame optical and NIR colors are dominated by an old stellar population, and that a comparatively low level of star formation is possible even on the "quiescent" side of the bimodal population.

7. IMPROVEMENTS ENABLED BY THE NIR MEDIUM-BAND FILTERS

Throughout this paper, we have emphasized the superior quality of the NMBS photometric redshifts and, consequently, rest-frame colors. Here, we provide a more comprehensive look at the improvements provided by medium-band filters compared to the standard broadband filters commonly used in high-redshift photometric surveys.

In Section 6, we isolated a sample of quiescent galaxies out to $z = 3.5$ from the NMBS using the rest-frame $U-V$ and $V-J$ colors. Although these galaxies span a large range of S/N, their spectral shapes will unambiguously contain strong Balmer/4000 Å breaks. This sample of galaxies is therefore ideal for characterizing the power of the NIR medium-band filters relative to the canonical broadband filters.

We have generated broadband catalogs in both fields with the same depth as the medium-band images as well as a broadband catalog with the deeper WIRDs *J* and *H* photometry. The WIRDS *J*- and *H*-band images have depths that are 1.2 and 2.3 mag deeper than the NMBS medium-band images in AEGIS (0.1 and 0.6 mag deeper in COSMOS), enabling us to test how depth affects the accuracies of the photometric redshifts. The images with the same depth as the NMBS survey were generated by combining the J_2 and J_3 medium-band images to create a *J*-band image ($J = (J_2 + J_3)/2$), and the H_1 and H_2 medium-band images for an *H*-band image ($H = (H_1 + H_2)/2$) for both fields. The broadband catalogs contain FUV/NUV, *ugriz*/*JHK* and IRAC photometry in both fields and we compare these to medium-band catalogs with FUV/NUV, *ugriz*/*JHK*, and IRAC photometry.

The photometric redshifts are fit for the medium-band and broadband catalogs using the same parameter settings and templates as described in Section 5. Figure 19 compares the median 68% confidence interval, $\langle\sigma/(1+z)\rangle$, of the photometric redshifts for all quiescent galaxies in the medium-band and broadband catalogs. The confidence intervals of photometric redshifts are appropriate given the true scatter in Figure 13 (at least for $z < 1$). It is therefore reasonable to believe them, and hence a comparison of confidence intervals for the larger sample is meaningful. We limit the sample to a completeness level of $\gtrsim$90%, with $K_{\rm tot} < 22.2$ mag. We note that the COSMOS field includes roughly twice as many optical filters as the AEGIS field, including the 12 Subaru optical medium-band filters. The additional deep optical broad and medium bands improve the confidence intervals of the COSMOS NMBS photometric redshifts at $z < 1$ by a factor-of-two, with little effect at $z > 1$. For simplicity, we restrict this analysis to only those filters included in both fields where we can strictly test the differences between a standard broadband catalog and the addition of the NIR medium-band filters.

The median 1σ confidence intervals of the broadband photometric redshifts of quiescent galaxies are up to a factor of two times greater than those calculated with the NIR medium-band

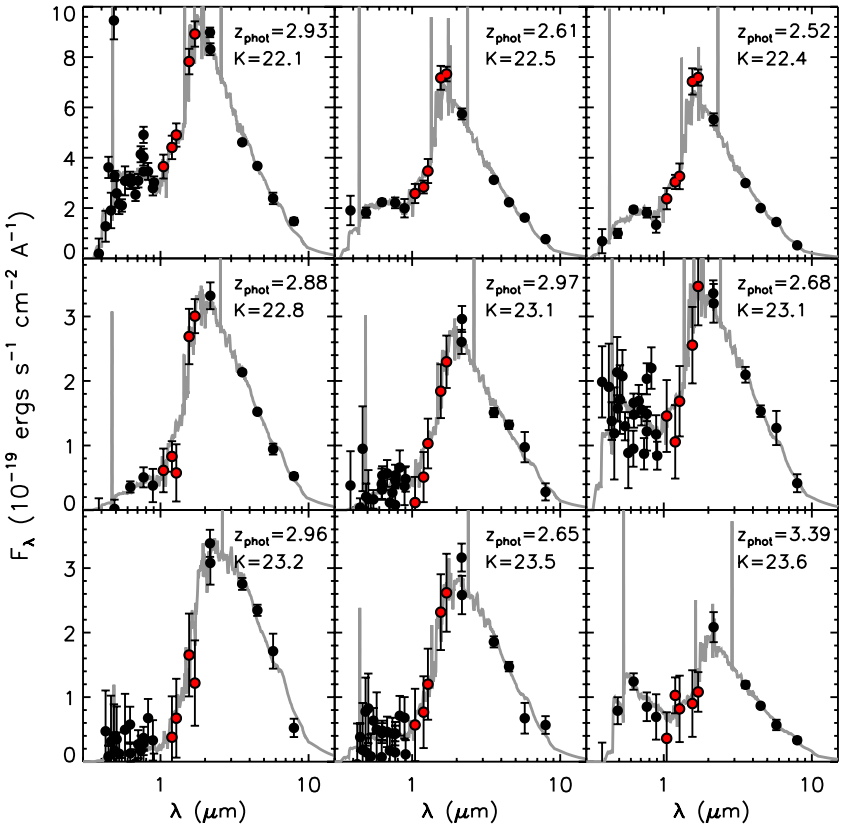

Figure 18. Example quiescent SEDs selected based on their $U-V$ and $V-J$ rest-frame colors from the highest redshift bin in Figure 17, sorted from bright to faint in K-band magnitude. The best-fit EAZY template is shown in gray and the medium-band filters in red. All of these galaxies show a prominent Balmer/4000 Å break.

(A color version of this figure is available in the online journal.)

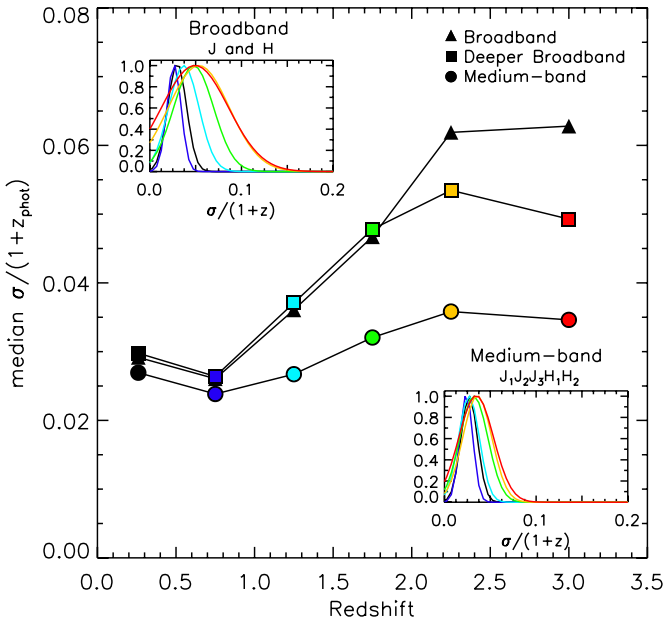

Figure 19. Median 68% confidence interval, $\langle\sigma/(1+z)\rangle$, of the photometric redshifts of quiescent galaxies selected by the *UVJ* rest-frame color selection technique. The confidence intervals are calculated for medium-band catalogs and broadband catalogs that replace the J_1, J_2, J_3, H_1, and H_2 medium-band filters with J and H filters.

(A color version of this figure is available in the online journal.)

filters. We note that the formal errors on the photometric redshifts will scale with the S/N of the detected objects, where the median 1σ confidence intervals will be smaller for brighter samples within the NMBS catalogs. For example, the typical 1σ confidence interval for a galaxy with $K_{\rm tot} = 18$–20 is 0.02, whereas this value increases to $\sim$0.04 for $K_{\rm tot} = 22$. The distribution of $\sigma/(1+z)$ for the quiescent sample within each redshift bin is roughly Gaussian; the inset panels in Figure 19 show the best-fit Gaussian distributions. The width of the distributions range from 0.01 to 0.02 for the medium-band catalogs, compared to a factor-of-two increase for the broadband catalogs.

The difference between the medium-band and broadband catalogs becomes more pronounced for those quiescent galaxies with $z > 1.5$, where the NIR medium-band filters start to sample the rest-frame Balmer/4000 Å break region. Figure 20 shows examples of quiescent galaxies ranging from $z = 0.27$ to $z = 2.91$ with the best-fit EAZY models smoothed with a Gaussian with a width of $0.15\,\mu{\rm m}/(1+z)$, the width of the medium-band filters. The rest-frame wavelength range that is sampled by the NIR medium-bandwidth filters (shown in red) shifts to shorter wavelengths toward higher redshift, beginning to sample the Balmer/4000 Å region at $z > 1.5$.

Figure 21 compares the median confidence intervals for the photometric redshifts of quiescent (red) and star-forming (blue) galaxies in the medium-band and broadband catalogs, as selected from the *UVJ* diagram in Figure 17. The difference between the broadband catalog and the addition of the NIR medium-band filters is most important for quiescent galaxies at $z > 1.5$. Deeper broadband photometry (squares in Figure 21) improves the errors at $z > 1.5$, but only to a certain degree. The formal errors will decrease as the error bars decrease with deeper photometry, but they seem to reach a floor around $\sigma/(1+z) \sim 0.05$, at which point increased spectral resolution is vital.

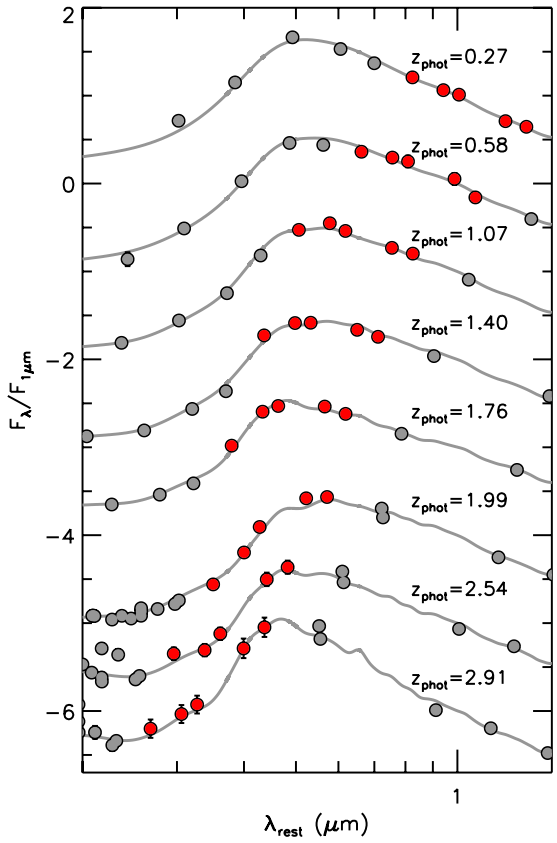

Figure 20. Examples of quiescent galaxies ranging from $z = 0.27$ to $z = 2.91$, showing the rest-frame wavelength range the NIR medium-bandwidth filters span (red) as a function of redshift. The best-fit EAZY models are smoothed with a Gaussian with a width of 0.15 μm/(1 + z), the resolution of the medium-band filters. The medium-band filters begin to sample the Balmer/4000 Å region at $z > 1.5$.

(A color version of this figure is available in the online journal.)

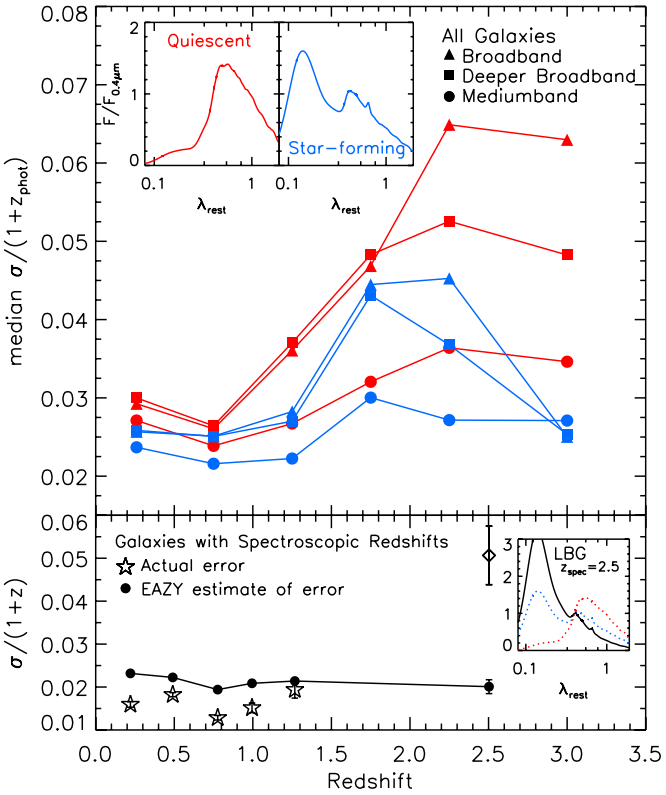

Figure 21. Median 68% confidence interval of the photometric redshifts of quiescent (red) and star-forming (blue) galaxies selected by the *UVJ* rest-frame color selection technique. The confidence intervals are calculated for both the medium-band and broadband catalogs. The top right inset panels show the difference between the average best-fit EAZY templates of the quiescent (left) and star-forming (right) galaxies, smoothed with a Gaussian to the resolution of the medium-band filters. The bottom panel shows the median confidence interval of only those galaxies with spectroscopic redshifts compared to the actual errors (stars) as determined from the photometric–spectroscopic comparison in Section 5, with the LBGs indicated separately as a diamond. The best-fit EAZY template for the sample of LBGs at $z_{spec} = 2.5$ is bluer than the average star-forming galaxy, with a weak Balmer/4000 Å break (see bottom right inset panel). The error for both quiescent and star-forming galaxies is up to a factor of two times smaller when using medium-band NIR data as compared to deep broadband data.

(A color version of this figure is available in the online journal.)

Quiescent and star-forming galaxies have different spectral shapes: the only prominent spectral feature in the spectrum of the quiescent galaxies is the Balmer/4000 Å break, whereas the star-forming galaxies typically have rest-frame UV emission with strong Lyman breaks. The top inset panels in Figure 21 show the spectral shape of the average best-fit EAZY template for the quiescent and star-forming galaxies, smoothed with a Gaussian to the resolution of the medium-band filters. We note that the decrease in the width of the confidence interval at $z = 3$ for the blue, star-forming galaxies for the broadband catalog is the result of the Lyman break shifting into the optical filter passbands.

The median confidence interval for the blue, star-forming galaxies are up to a factor of ∼1.5 smaller than for the red, quiescent galaxies for the catalog that includes the medium-band filters. The medium-band filters provide more similar photometric redshift uncertainties for the quiescent and star-forming samples (i.e., they reduce the huge divergence seen at $z > 2$ for standard broadband filters), which can be important for clustering analyses. We note that the average blue, star-forming galaxy still has a well-developed Balmer/4000 Å break, which is why the medium-band filters help even for those galaxies. Additionally, the deep optical broadband data will help constrain the photometric redshifts for those galaxies with rest-frame UV emission.

van Dokkum et al. (2006) showed that the "median galaxy" at $2 < z < 3$ with mass $> 10^{11}\,M_\odot$ is faint in the observer's optical, red in the observed NIR, and has a rest-frame UV spectrum that is relatively flat in F_λ. Therefore, the typical massive high-redshift galaxy can either have a spectral shape similar to quiescent galaxies or that of a red, dusty galaxy. For both cases, Figure 21 demonstrates that the NIR medium-bandwidth filters are necessary to improve the confidence intervals of the photometric redshifts of the typical massive high-redshift galaxy. In fact, the photometric redshifts are more accurate when including the NIR medium-band filters regardless of the spectral shape.

In addition to comparing photometric redshift confidence intervals, we can also look at how the fraction of catastrophic outliers and the overall accuracy of those galaxies with spectroscopic redshifts changes in both fields when using the broadband catalogs versus the medium-band catalogs. We find that the fraction of catastrophic outliers increases by a factor of two in COSMOS when using only broadband filters with similar depth to the NMBS survey. By increasing the depth of the *J*- and *H*-band images by 1–2 mag, as is the case with the AEGIS WIRDS data, the fraction of catastrophic outliers is the same as that resulting from the medium-band photometry.

The scatter, $\sigma_z/(1+z)$, increases by 15% and 30% in COSMOS and AEGIS for the deeper broadband catalogs, respectively, consistent with the EAZY estimate of the errors at these redshifts (see Figure 21).

We note that the EAZY confidence intervals are not well calibrated. To test how representative the 68% confidence intervals of the photometric redshifts are of the actual errors, we consider the subsample of galaxies with spectroscopic redshifts. In the bottom panel of Figure 21, we compare the actual errors from the photometric–spectroscopic redshift comparison in Section 5 to the median confidence intervals. At $z < 1.5$, the EAZY error tends to overestimate the actual error by ∼20%–40%. On the other hand, the sample of LBGs at $z > 1.5$ has actual errors that are almost a factor of three times larger than the EAZY errors (diamond in bottom panel of Figure 21). We note that the LBGs have spectral shapes different from the majority of NMBS galaxies (see the bottom right inset panel in Figure 21), with weak Balmer/4000 Å breaks and very faint *K*-band magnitudes. The median *K*-band magnitude of the sample of LBGs with spectroscopic redshifts is 23.9 mag, compared to a median *K*-band magnitude of 22.2 mag for the sample of galaxies with $z_{\rm spec} < 1.5$ (see also Figure 14). For brighter *K*-band magnitude limits at $z > 1.5$, we currently have very limited spectroscopic information (see Section 5).

8. SUMMARY

We present the relatively deep and wide medium-band NIR imaging of the NMBS survey, consisting of two ∼0.21 deg^2 fields within the AEGIS and COSMOS surveys. The observations were carried out as part of a NOAO Survey Program on Mayall, using the NEWFIRM camera with five NIR medium-bandwidth filters. The full details of the observations and data reduction are described in Sections 2.2 and 3, respectively, including various optimizations to the images to improve the image quality. The astrometry is accurate within $\lesssim$0.″1 (0.3 pixels). The final combined images are constructed from individually registered, distortion-corrected weighted averages of all frames; the flatness of the background and excellent quality of the data is readily apparent in Figures 3 and 4. The reduced NMBS images and weight maps are publicly available through the NOAO archive and through the NMBS site.

We combined the NMBS data with UV (*GALEX*), visible (CFHT and Subaru), NIR (CFHT), and mid-IR (*Spitzer*/IRAC) data to produce a public *K*-selected photometric catalog, which we make available to the community.[26] Since about 10% of the objects detected by SExtractor are clearly blended objects (for example, see Figure 8), we use custom scripts to deblend the objects using a higher resolution *K*-band image. The deblended catalog is included in addition to the original list of objects identified using SExtractor. With the NMBS catalogs, we summarize our main findings as follows.

1. The NMBS catalogs contain ∼13,000 galaxies at $z > 1.5$ with accurate photometric redshifts and rest-frame colors. We demonstrate the excellent quality of the NMBS SEDs throughout this paper (see also van Dokkum et al. 2009, 2010; Brammer et al. 2009; Whitaker et al. 2010; Kriek et al. 2010, 2011; Marchesini et al. 2010; Brammer et al. 2011).
2. We find excellent agreement with available spectroscopic redshifts, with $\sigma_z/(1+z) \sim 0.008$ for 1509 galaxies in COSMOS and $\sigma_z/(1+z) \sim 0.017$ for 2525 galaxies in AEGIS. It should be noted that the currently available spectroscopic samples are heavily weighted toward blue, low-redshift galaxies. Several programs for follow-up spectroscopy of NMBS targets at $z > 1.5$ are currently underway.
3. We show evidence of a clear bimodal color distribution between quiescent and star-forming galaxies persisting to $z \sim 3$, a higher redshift than has been probed before.
4. The median 68% confidence intervals of the photometric redshifts for both quiescent and star-forming galaxies is up to a factor of two times smaller when comparing medium-band catalogs to broadband catalogs due to the increased resolution of the five NIR medium-band filters.

Follow-up programs will continue to add to the legacy of the survey as our understanding of these high-redshift galaxies grows and evolves. Calibrations of the medium-band photometric redshifts at $1 < z < 3.5$ will be possible with the upcoming *HST* Treasury program, 3D–*HST*. This NIR spectroscopic survey will partially overlap with the NMBS fields.

We thank the anonymous referee for useful comments and a careful reading of the paper. This paper is based partly on observations obtained with MegaPrime/MegaCam, a joint project of CFHT and CEA/DAPNIA, and WIRCam, a joint project of CFHT, Taiwan, Korea, Canada, and France at the CFHT, which is operated by the National Research Council (NRC) of Canada, the Institut National des Science de l'Univers of the Centre National de la Recherche Scientifique (CNRS) of France, and the University of Hawaii. This work is based in part on data products produced at TERAPIX, the WIRDS consortium, and the Canadian Astronomy Data Centre. We thank H. Hildebrandt for providing the CARS-reduced CFHTLS images. This study also makes use of data from AEGIS, a multiwavelength sky survey conducted with the *Chandra*, *GALEX*, *Hubble*, Keck, CFHT, MMT, Subaru, Palomar, *Spitzer*, VLA, and other telescopes and supported in part by the NSF, NASA, and the STFC. Support from NSF grant AST-0807974 and NASA grant NNX11AB08G is gratefully acknowledged.

Facilities: Mayall (NEWFIRM)

REFERENCES

Baldry, I. K., Glazebrook, K., Brinkmann, J., Ivezić, Ž., Lupton, R. H., Nichol, R. C., & Szalay, A. S. 2004, ApJ, 600, 681
Barmby, P., Huang, J., Ashby, M. L. N., Eisenhardt, P. R. M., Fazio, G. G., Willner, S. P., & Wright, E. L. 2008, ApJS, 177, 431
Baugh, C. M. 2006, Rep. Prog. Phys., 69, 3101
Bertin, E., & Arnouts, S. 1996, A&AS, 117, 393
Brammer, G. B., van Dokkum, P. G., & Coppi, P. 2008, ApJ, 686, 1503
Brammer, G. B., et al. 2009, ApJ, 706, L173
Brammer, G. B., et al. 2011, ApJ, submitted (arXiv:1104.2595)
Capak, P., et al. 2007, ApJS, 172, 99
Capak, P., et al. 2008, VizieR Online Data Catalog, 217, 20099
Cassata, P., et al. 2008, A&A, 483, L39
Cimatti, A., et al. 2002, A&A, 392, 395
Conroy, C., Gunn, J. E., & White, M. 2009, ApJ, 699, 486
Conroy, C., White, M., & Gunn, J. E. 2010, ApJ, 708, 58
Daddi, E., et al. 2005, ApJ, 626, 680
Davis, M., et al. 2003, Proc. SPIE, 4834, 161
Davis, M., et al. 2007, ApJ, 660, L1
Dickinson, M., Papovich, C., Ferguson, H. C., & Budavári, T. 2003, ApJ, 587, 25
Erben, T., et al. 2009, A&A, 493, 1197

[26] www.astro.yale.edu/nmbs

Fioc, M., & Rocca-Volmerange, B. 1999, arXiv:astro-ph/9912179
Fontana, A., et al. 2006, A&A, 459, 745
Förster Schreiber, N. M., et al. 2006, AJ, 131, 1891
Franx, M., et al. 2003, ApJ, 587, L79
Franzetti, P., et al. 2007, A&A, 465, 711
Giallongo, E., Salimbeni, S., Menci, N., Zamorani, G., Fontana, A., Dickinson, M., Cristiani, S., & Pozzetti, L. 2005, ApJ, 622, 116
Hildebrandt, H., Pielorz, J., Erben, T., van Waerbeke, L., Simon, P., & Capak, P. 2009, A&A, 498, 725
Ilbert, O., et al. 2009, ApJ, 690, 1236
Kauffmann, G., et al. 2003, MNRAS, 341, 33
Kriek, M., van der Wel, A., van Dokkum, P. G., Franx, M., & Illingworth, G. D. 2008a, ApJ, 682, 896
Kriek, M., van Dokkum, P. G., Whitaker, K. E., Labbe, I., Franx, M., & Brammer, G. B. 2011, arXiv:1103.0279
Kriek, M., et al. 2006, ApJ, 649, L71
Kriek, M., et al. 2008b, ApJ, 677, 219
Kriek, M., et al. 2010, ApJ, 722, L64
Kron, R. G. 1980, ApJS, 43, 305
Kroupa, P. 2001, MNRAS, 322, 231
Labbé, I., Bouwens, R., Illingworth, G. D., & Franx, M. 2006, ApJ, 649, L67
Labbé, I., et al. 2003, AJ, 125, 1107
Labbé, I., et al. 2005, ApJ, 624, L81
Labbé, I., et al. 2007, ApJ, 665, 944
Laidler, V. G., et al. 2007, PASP, 119, 1325
Lilly, S. J., et al. 2007, ApJS, 172, 70
Lupton, R., Gunn, J. E., Ivezić, Z., Knapp, G. R., & Kent, S. 2001, in ASP Conf. Ser. 238, Astronomical Data Analysis Software and Systems X, ed. F. R. Harnden, Jr., F. A. Primini, & H. E. Payne (San Francisco, CA: ASP), 269
Maíz Apellániz, J. 2006, AJ, 131, 1184
Maraston, C. 2005, MNRAS, 362, 799
Marchesini, D., van Dokkum, P. G., Förster Schreiber, N. M., Franx, M., Labbé, I., & Wuyts, S. 2009, ApJ, 701, 1765
Marchesini, D., et al. 2010, ApJ, 725, 1277
Markwardt, C. B. 2009, in ASP Conf. Ser. 411, Astronomical Data Analysis Software and Systems XVIII, ed. D. A. Bohlender, D. Durand, & P. Dowler (San Francisco, CA: ASP), 251
Martin, D. C., et al. 2005, ApJ, 619, L1
McCracken, H. J., et al. 2010, ApJ, 708, 202
Muzzin, A., Marchesini, D., van Dokkum, P. G., Labbé, I., Kriek, M., & Franx, M. 2009, ApJ, 701, 1839
Olsen, L. F., et al. 2007, A&A, 461, 81
Pickles, A. J. 1998, PASP, 110, 863
Quadri, R., et al. 2007, AJ, 134, 1103
Reddy, N. A., Steidel, C. C., Pettini, M., Adelberger, K. L., Shapley, A. E., Erb, D. K., & Dickinson, M. 2008, ApJS, 175, 48
Sanders, D. B., et al. 2007, ApJS, 172, 86
Schlegel, D. J., Finkbeiner, D. P., & Davis, M. 1998, ApJ, 500, 525
Scoville, N. 2007, in ASP Conf. Ser. 375, From Z-Machines to ALMA: (Sub)Millimeter Spectroscopy of Galaxies, ed. A. J. Baker, J. Glenn, A. I. Harris, J. G. Mangum, & M. S. Yun (San Francisco, CA: ASP), 166
Steidel, C. C., Adelberger, K. L., Giavalisco, M., Dickinson, M., & Pettini, M. 1999, ApJ, 519, 1
Steidel, C. C., Adelberger, K. L., Shapley, A. E., Pettini, M., Dickinson, M., & Giavalisco, M. 2003, ApJ, 592, 728
Steidel, C. C., Giavalisco, M., Pettini, M., Dickinson, M., & Adelberger, K. L. 1996, ApJ, 462, L17
Taniguchi, Y., et al. 2007, ApJS, 172, 9
Taylor, E. N., et al. 2009a, ApJ, 694, 1171
Taylor, E. N., et al. 2009b, ApJS, 183, 295
van Dokkum, P. G., & Franx, M. 1996, MNRAS, 281, 985
van Dokkum, P. G., et al. 2006, ApJ, 638, L59
van Dokkum, P. G., et al. 2009, PASP, 121, 2
van Dokkum, P. G., et al. 2010, ApJ, 709, 1018
Wake, D. A., et al. 2011, ApJ, 728, 46
Whitaker, K. E., et al. 2010, ApJ, 719, 1715
Williams, R. J., Quadri, R. F., Franx, M., van Dokkum, P., & Labbé, I. 2009, ApJ, 691, 1879
Wittman, D. 2009, ApJ, 700, L174
Wolf, C., Meisenheimer, K., Rix, H., Borch, A., Dye, S., & Kleinheinrich, M. 2003, A&A, 401, 73
Wuyts, S., et al. 2007, ApJ, 655, 51
Zamojski, M. A., et al. 2007, ApJS, 172, 468